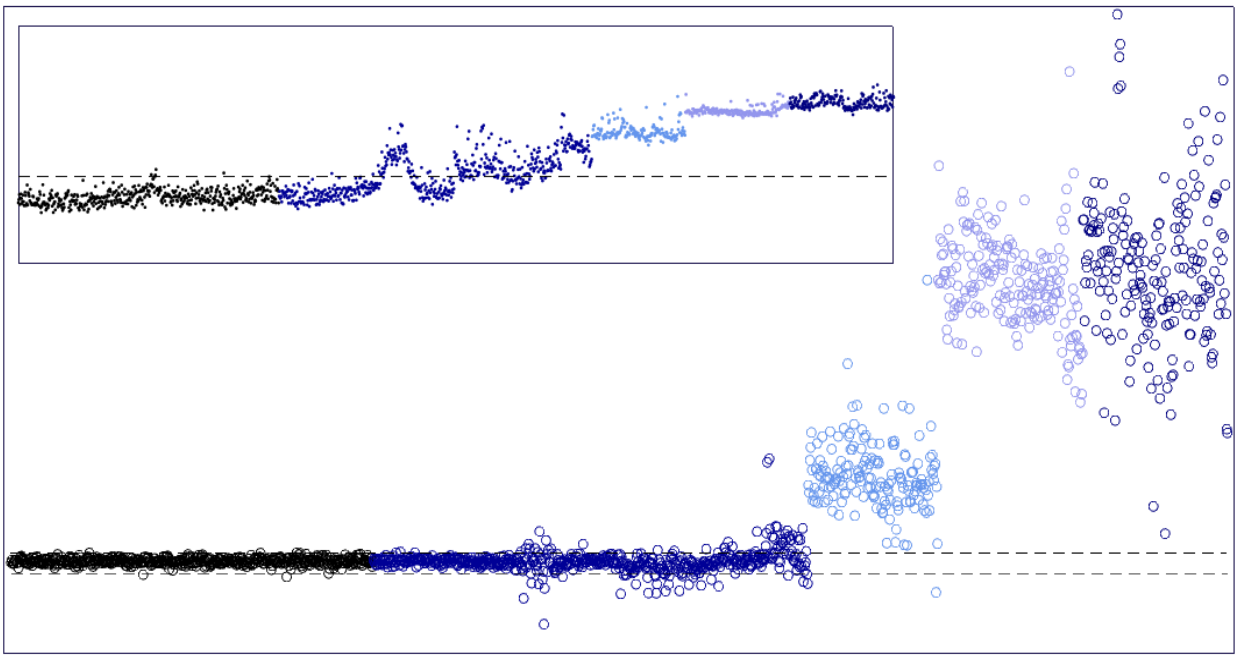

VIBRATION-BASED DAMAGE DETECTION

WITH FOCUS ON MITIGATING ENVIRONMENTAL AND OPERATIONAL VARIABILITIES THROUGH COINTEGRATION

Juan Carlos Burgos Díaz

Mechanical Design, BM4-3, 2020-06

Master's Project

VIBRATION-BASED DAMAGE DETECTION

WITH FOCUS ON MITIGATING ENVIRONMENTAL AND OPERATIONAL VARIABILITIES THROUGH COINTEGRATION

Juan Carlos Burgos Díaz

Mechanical Design, BM4-3-F19, 2020-06

Master's Project

Structural and Civil Engineering
Aalborg University
http://www.aau.dk

AALBORG UNIVERSITY
STUDENT REPORT

Title:
Vibration-Based Damage Detection

Theme:
Structural Damage Detection

Project Period:
September 2019 - June 2020

Project Group:
BM4-3

Participant(s):
Juan Carlos Burgos Díaz

Supervisor(s):
Martin Dalgaard Ulriksen
Bilal Ali Qadri

Copies: 1

Page Numbers: 56

Date of Completion:
June 10, 2020

Abstract:

The objective of a vibration-based structural damage detection approach is to ascertain if damage is present or not in a structure based on measured vibration signals. In reality, structures are subject to changing environmental and operational conditions that affect the measured vibration signals, and these ambient variations can often mask subtle changes in the measured vibration signals caused by damage. The mitigation of the influence of these ambient variations is one of the main challenges for the implementation of a damage detection approach on structures in service. This thesis addresses that challenge through the application of cointegration. Its application is investigated through numerical and experimental studies.

Contents

Preface

The thesis has been completed during a long Master's Thesis of the Master's programme in Mechanical Design at Aalborg University Esbjerg, from September 2019 to June 2020. The theme of the thesis is within the field of vibration-based structural damaged detection with the application of cointegration to mitigate the influences of environmental and operational variabilities. The theme should address readers from the field of Mechanical, Civil and Structural Engineering, and others interested in the field of structural damaged detection.

Acknowledgments

I would first like to thank my thesis supervisor Dr. Martin Dalgaard Ulriksen, Assistant Professor in the Department of Energy Technology at Aalborg University. He was always willing to answer my questions and support my research. His guidance kept me in the right direction and his comments were an invaluable contribution to my thesis. Furthermore, I would like to express my gratitude M.Sc Bilal Ali Qadri, Research Assistant at the same department. He introduced me to the topic of structural damage detection and supported me in the research and on the development of the simulations for this project.

I wish to thank Dr. Dmitri Tcherniak, Research Engineer at Bruel & Kjaer Sound and Vibration Measurement A/S, for allowing access to the data and figures used in this thesis.

I am also thankful to my classmates for their support in my studies, and to my dear friends for making me feel at home during these two years of education.

Finally, I must express my endless gratitude to my sister and parents for their advice and continuous encouragement, without which this project would not have been possible. Thank you!

Aalborg University, June 10, 2020

Juan Carlos Burgos Díaz
<jburgo18@student.aau.dk>

Chapter 1

INTRODUCTION

The process of implementing a damage detection strategy for a structure is referred as structural health monitoring (SHM). In this context damage is defined as changes to the material and/or geometric properties of these systems, including changes to the boundary conditions and system connectivity, which adversely affect the system's performance [7].

Damage detected in its early stage can avoid unnecessary shutdowns of in-service structures and decrease maintenance cost. SHM is used to monitor the condition of the structures to provide, in real time, information regarding its integrity [7]. The evaluation of this information can give an alarm of an early stage of damage, and allows to take immediate action before any harmful or no repairable situation arises.

A SHM system consist of four levels. The first three levels are detection, localization and quantification of any damage. These three levels are known as diagnosis. The fourth level involves the assessment of the consequences of the diagnosed damaged and is known as prognosis.

The first level is referred as structural damage detection (SDD). In this level the objective is to ascertain if damage is present or not in the structure. This thesis deals with the implementation of an approach for SDD through the use of measured vibration signals from the structure.

1.1 VIBRATION-BASED STRUCTURAL DAMAGE DETECTION

Damage in a structure is typically associated with changes in mass, stiffness or damping properties of the system. These characteristic of damage, in turn, change the vibrational characteristics of the structure [5, 6]. Then the presence of damage can be evaluated from the analysis of the damaged-induces changes in the vibration responses of the structure.

Since sensors cannot measure damage, an adequate vibration-based SDD approach is required to transform the vibration measurement responses into damage-sensitive information that can be used to asses the presence of damage. Different approaches have demonstrated

promising results in experimental studies [14].

However, the implementation of vibration-based SDD approaches in realistic application presents several challenges, among them: defining the number and proper location of the sensors, extraction of damage-sensitive information and discriminate damage-induced changes from changes induced by changing environmental and/or operational conditions.

Environmental variabilities (EVs) as wind, temperature, rain, snow, humidity and waves, and operational variabilities (OVs) as loading conditions and operational speed affect the vibration responses of the structure. This influence, arise a problem that need to be faced by the SDD approach.

1.2 STATEMENT OF THE PROBLEM

The environmental and operational variabilities (EOVs) induced changes are among the main obstacles to implement vibration-based SDD on structures in service. EOVs influence can mask the changes actually caused by damage on the vibration responses or can lead to false indications of damage. For that reason, it is important to investigate an approach to remove or at least mitigate the influence of EOVs in vibration-based SDD.

1.3 THESIS SCOPE

This thesis investigates the use of cointegration, a technique from the field of econometrics, to remove or at least mitigate the EOVs influences in SDD results. To this end, numerical and experimental case studies are performed. The experimental case study is based on actual data for an operating Vestas V27 wind turbine, which allows for evaluation of the approach under real EOVs conditions.

1.4 THESIS OUTLINE

Five chapters follow this introduction, the outline of their content is given below:

Chapter 3 In this chapter, the principles of the outlier analysis method are presented together with its application for SDD. After, Mahalanobis square distances and cointegration are introduced. These techniques are used as metric for the implementation of outlier analysis approach in SDD.

Chapter 4 In this chapter, the outlier analysis method and techniques introduced in chapter 3 are applied to numerical simulations. These simulations emulates different scenarios of EOVs in order to validate the use of the outlier analysis approach.

Chapter 5 The fifth chapter deals with an experimental application. Data from an operating Vestas V27 wind turbine is used in order to verify if the outlier analysis based on cointegration can remove or at least mitigate EOVs influences in the results.

Chapter 6 In the last chapter the discussion and conclusions are presented, followed by suggestions for future research in this topic.

Chapter 2

DAMAGE DETECTION METHODS

The goal of any SDD approach is to classify the current state of a structure as undamaged or damaged. Damage alters the stiffness, mass and/or damping properties of a structure, which, in turn, will change the measured dynamic response of the system [5, 6] with respect to its undamaged state. Then, from the analysis of the vibration responses, it would be possible to classify the current state of the structure as undamaged or damaged. Outlier analysis [17, 21, 22] is one of the methods used to reach this goal.

2.1 OUTLIER ANALYSIS PRINCIPLES

The outlier analysis method is a statistical method used to evaluate an observation as consistent or inconsistent with a reference state of the data. For this, a baseline model is constructed with a group of observations that represent the reference state, which are also known as training observations. Any current observation is compared against the baseline model; if the current observation is consistent with the baseline model it is classified as an inlier; if not, it is classified as an outlier to the baseline model.

To perform outlier analysis, a variable or set of variables that represented the state of the data at each observation are selected. Each of these variables is known as feature.

For data, which state can be represented for two features X_1 and X_2, the principles behind the outlier analysis method are depicted as in figure 2.1. Each pair of values represents a particular observation. The ellipse represents the threshold of the baseline model, all the observations inside the ellipse are classified as inliers, and the observations outside the ellipse are classified as outliers to the baseline model.

Figure 2.2 represents a more complicated case, where some observations that are consistent with the baseline model, circular marks, are allowed to be outside the threshold. This tolerance is typically needed to avoid a high number of observations that are not consistent with the baseline model, square marks, be placed inside the threshold. For example, if the elliptical threshold is enlarged to include all circular marks, the number of square marks inside it will increase up to five.

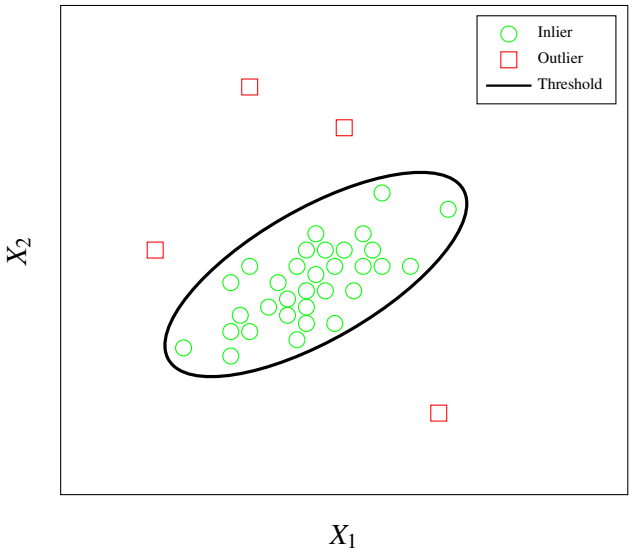

Figure 2.1: Outlier analysis representation for two features data.

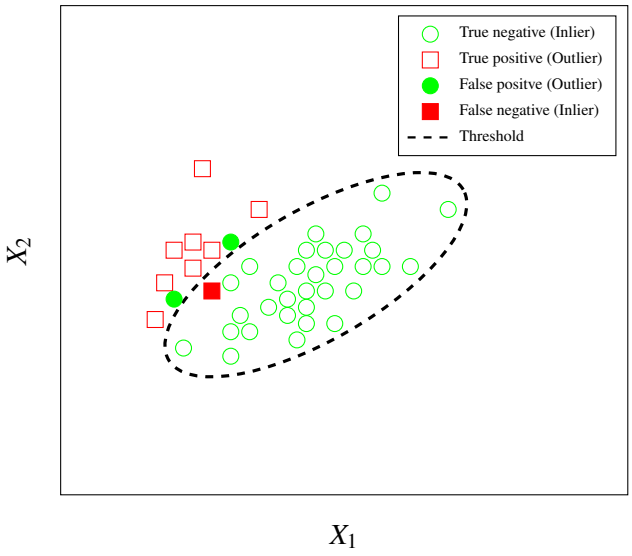

Figure 2.2: Outlier analysis representation for two features data, with allowed tolerance for the threshold.

A false positive is an observation that is consistent with the reference state that is labeled as an outlier; see figure 2.2. Conversely, a false negative is an observation that is not consistent with the reference state that is labeled as an inlier. Following this description, a true negative is an inlier observation that is consistent with the baseline model, and a true positive is an outlier observation that is not consistent with the baseline model. To select the threshold a percentage of false positives in the baseline model is allowed to avoid a high

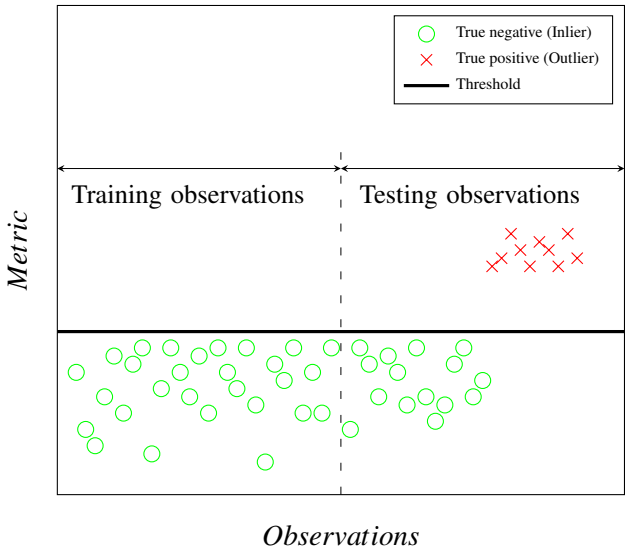

Figure 2.3: Representation of outlier analysis using a metric that projects multivariate features to a one-variate representation.

percentage of false negatives. Current states of the data, represented by testing observations, are compared against this selected threshold.

Metric is the technique used to measure the discordancy of the observations with respect to the baseline model. It allows the observations to be judged to be statistically likely or unlikely to have come from the baseline model [22]. For data characterized by more than three features, it is difficult to graphically represent the observations and evaluate the discordancy respect to the baseline model. In this case, one can use a metric that projects the multivariate feature to a one-variate representation for each observation, as is shown in figure 2.3.

The baseline model is constructed with metrics computed from training observations that corresponds to the reference state of the data, and a threshold value is selected allowing a percentage of false positives, as depicted in figure 2.4.

The metric of the testing observations, under evaluation, is compared against the threshold defined from the training observations. In this manner, the observations are classified as inliers or outliers respect to the baseline model.

2.1.1 PERFORMANCE INDICATORS

Evaluation of the outlier analysis approach can be accomplished based on the number of false positives and true positives obtained from the testing observations classification.

The evaluation of the selected false positive allowance, that is used to compute the threshold, is done with two ratios, the false-positive rate (FPR) and the true-positive rate (TPR). FPR is computed as the ratio of false positives to the sum of false positives plus true

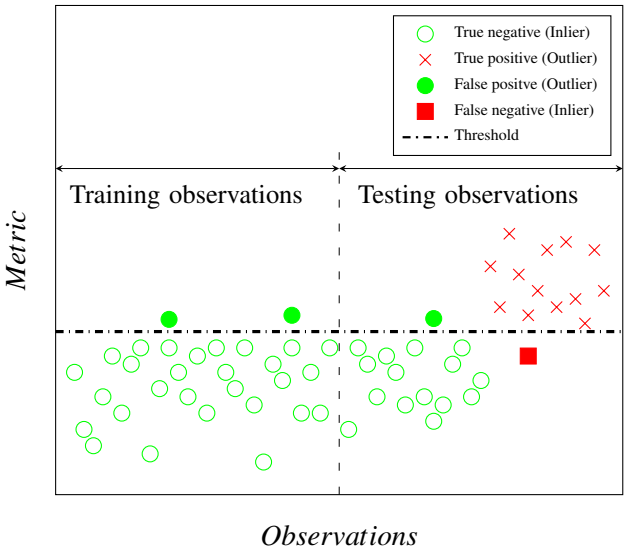

Figure 2.4: Representation of outlier analysis for multivariate features projected to a one-variate representation, with threshold based on false positive allowance.

negatives in the testing observations. TPR is computed as the ratio of true positives to the sum of true positives plus false negatives in the testing observations, see figure 2.4.

The whole evaluation of the outlier analysis approach is done calculating TPR and FPR for the whole range of thresholds, that is for all values of false positives that can be allowed in the training observations (0% to 100%). Plotting the TPR against FPR results gives the receiver operating characteristic curve (ROC), see Figure 2.5. This curve allows evaluating the implemented outlier analysis approach. An approach that performs a perfect classification always detects 100% of true positives in the testing observations for any selected threshold. It has the area under the ROC curve (AUC) equal to one [20]. A good approach has AUC near one. Approaches with AUC equal to or lower than 0.5 are poor. An approach with AUC equal to 0.5 gives random results, it is not able to classify the testing observations. An approach with AUC lower than 0.5 classifies the testing observations incorrectly, classifying true negatives as true positives and vise versa.

To perform outlier analysis for damage detection in SDD, a feature or set of features together with a metric are required. The features represent the state of the structure at each observation. The metric evaluates the features with respect to the reference state of the structure.

2.1.2 FEATURES FOR SDD

Feature in SDD is a damage-sensitive property or properties extracted from the sensor measurement responses. It is used to represent the state of the structure at each observation, and it can allow to distinguish between the undamaged and the damaged states of the struc-

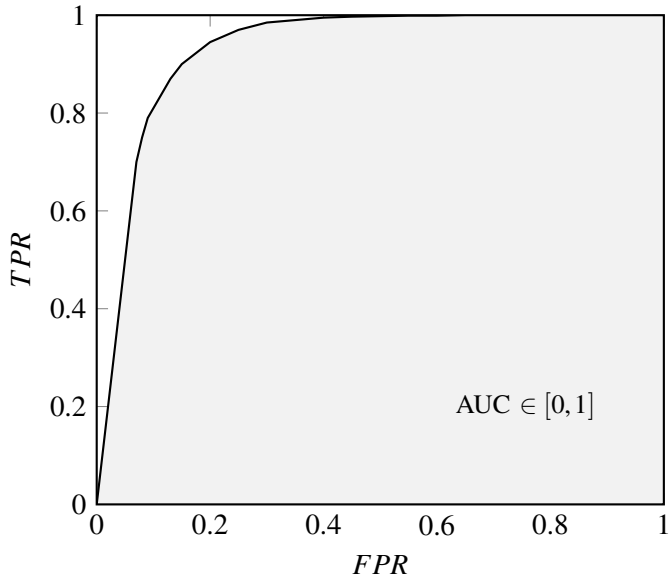

Figure 2.5: Receiver operating characteristic curve (ROC)

ture [7]. The selection of the feature requires special attention [23]. The feature must be as sensitive to damage as possible, and still, at the same time, insensitive to other variable conditions that can mask damage-induced changes in the measurement responses, see section 2.1.4. That is a compromise between both requirements.

In this thesis, all measurement responses and features are real values, and each feature is a set of properties group into a vector $\mathbf{x} \in \mathbb{R}^p$, where p is the dimension of the feature.

At each observation, the state of the structure is represented with a feature. The problem is to find a reduced dimension quantity that depends on the damage [23], but not on other variable conditions. Several options from vibration time-series responses have been tested, for example, unique elements of covariances matrices between responses [17], major components from principal component analysis of the responses [21], selected frequencies points of the transmissibility function between responses [22], selected frequencies points of the power spectra of the response [22], auto-regressive coefficients of the responses [7, 16], and modal parameters estimated from the response [12].

The selection of the most appropriate feature depends on each application, there is not an optimal feature for all the problems, even for the same problem, different options are possible. For this reason, it is essential to tailor the feature selection to the specific problem, based on engineering judgment, with the goal of preserving the information from damage [23] and to reduce the influence of other variable conditions.

In SDD, the reference state is the undamaged state of the structure. Training features, from training observations, represent the undamaged state and are used to construct the baseline model. Testing features, from testing observations, represent the states of the structure being evaluated against the baseline model. If a testing feature is consistent with the baseline

model, the state of the structure is classified as undamaged. If not, it is classified as damaged. To perform such classification, an adequate metric to measure the discordancy with respect to the baseline model is required.

2.1.3 METRICS FOR SDD

To classify the structure as damage or undamaged, it is necessary to measure the discordancy of the multivariate features with respect to the baseline model. The Mahalanobis square distance can be used as a metric to this end. It is described in section 2.2.

Cointegration is an approach that can be used to represent the baseline model and to investigate the discordance of multivariate features. And it can mitigate the influence of environmental and operational conditions on the features. It is described in section 2.3.

2.1.4 INFLUENCE OF EOVs

Environmental conditions as wind, temperature, rain, and operational conditions as machine speed, loading, among others under which in-service structures operate, affect the response signals. These varying conditions can often mask the subtle changes in the structure's vibration responses caused by damage [15], producing false positive indications of damage which could erode confidence in the SDD approach [7]. The problem increases when measurements of the EOVs are not available, as is usually the case for real structures.

To mitigate the influence of EOVs in SDD procedures, one approach that has been used is data normalization [7]. For instance, the response signals can be normalized by the measured inputs or the features can be normalized by a characteristic of the responses. However, for the success of this approach, training datasets must be collected over a wide range of EOVs. Otherwise, abnormal environmental and operational conditions can have similar effects as that of damage [15]. Furthermore, if the changes in the features caused by EOVs produces similar changes to those caused by damage, it will be necessary to measure the variability source to detect damage [7].

Cointegration is being used to mitigate the influence of EOVs [1, 2, 4]. In this approach, the monitored features are treated to remove their common trend caused by EOVs in the measurements. This is the approach investigated in this thesis and it is described in section 2.3.

2.2 MAHALANOBIS SQUARE DISTANCE

For a univariate feature ($p = 1$), the deviation statistics can be used as metric [22], equation 2.1, where Z_ζ is the discordance value, X_ζ is the feature being evaluated as a potential outlier, and $\overline{X}$ and S are the mean and standard deviation of the n_{tr} training features corresponding to the baseline model.

$$Z_\zeta = \frac{|X_\zeta - \overline{X}|}{S} \tag{2.1}$$

For a multivariate feature, with feature dimension $p > 1$, the equivalent of equation 2.1 is the Mahalanobis square distance measure [22], given by equation 2.2. The baseline model is represented by the mean $\overline{\mathbf{x}} \in \mathbb{R}^p$ and the covariance matrix $\mathbf{S} \in \mathbb{R}^{p\times p}$ of the n_{tr} training features $\mathbf{X}_{tr} \in \mathbb{R}^{p\times n_{tr}}$, and $\mathbf{x}_\zeta \in \mathbb{R}^p$ is the feature under evaluation.

$$D_\zeta = \left(\mathbf{x}_\zeta - \overline{\mathbf{x}}\right)^T [\mathbf{S}]^{-1} \left(\mathbf{x}_\zeta - \overline{\mathbf{x}}\right) \tag{2.2}$$

The mean and covariance matrix are evaluated as exclusive measurements, meaning that the feature under evaluation $\mathbf{x}_\zeta$ is not taken into account for their calculation. It is because the healthy state of the structure is known beforehand, then the Mahalanobis square distances are computed as exclusive values from the training observations. This allows computing the baseline model without contaminating its statistic with a potential damage feature from the testing state.

The use of Mahalanobis square distances as a metric requires two assumptions. First, the features used to compute the baseline model must have normal distribution [22], $\mathbf{X}_{tr} \sim N(\overline{\mathbf{x}}, \mathbf{S})$; that is, they must have time-invariant $\overline{\mathbf{x}}$ and $\mathbf{S}$, this assumption will not generally be true. However, if the deviations from the normal distribution are small, the outlier analysis can work adequately [7]. Small deviations from the normal distribution mean that the distribution has a clear most frequent value, and it has appropriately weighted tails. Second, it must be possible to construct a training data set that contains only healthy states of the structure[22]. To accomplish this assumption, the training observations must be obtained when it is known that the structure is in its undamaged state, for instance, at the beginning of the service. All the examples and experiments in this thesis comply with the last assumption.

In the context of SDD, if the Mahalanobis square distance of a damage-sensitive feature exceeds the threshold, it means that the current state of the structure does not correspond to the reference state. In principle, this implies that damage has occurred, but one has to ensure that the change in the feature is not governed by EOVs [23].

2.3 COINTEGRATION

Cointegration is a technique from the field of econometrics. It identifies long term relationships (trends) among non-stationary time series [9]. Hence, it can be used to detrend the common dependence on one or more unmeasured factors from these time series.

Stationary time series have a well defined mean and variance that do not change over time [10]. By contrast, non-stationary time series do not fulfil this requirement. If two or more non-stationary time series are cointegrated, they can be linearly combined to make a stationary time series from which the common trends of the original non-stationary series have been purged [3]. This concept can be illustrated by taking the two non-stationary time

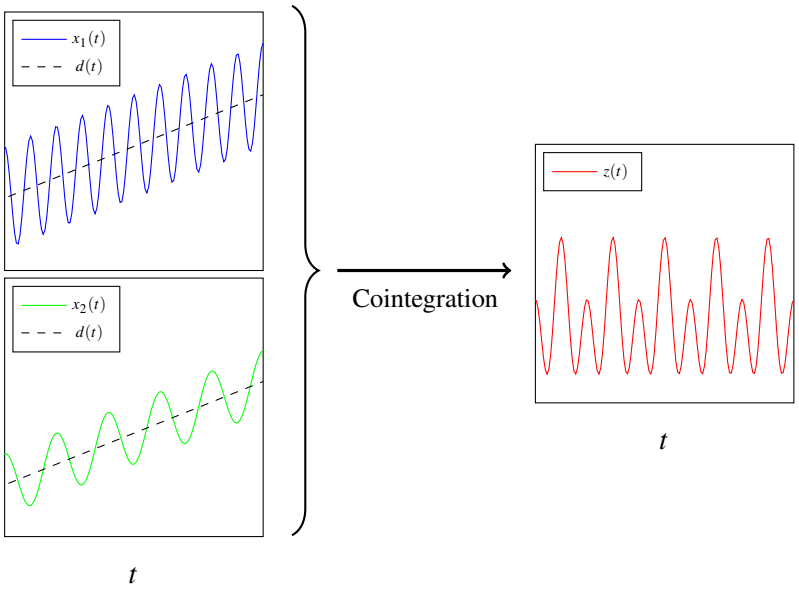

Figure 2.6: Non-stationary time series $x_1(t)$ and $x_2(t)$ are cointegrated into a stationary linear combination $z(t)$

series of equation 2.3, where the common trend is represented by $d(t) = t$, and the parameters f_i and a_i $\forall i \in [1,\ 2]$ are the amplitudes and frequencies of the cosine functions. The stationary linear combination $z(t)$ of these time series is obtained subtracting one time series from the other, equation 2.4. This stationary linear combination does not content the common trend $d(t)$ of the non-stationary time series. A graphical representation is shown in figure 2.6.

$$\begin{aligned} x_1(t) &= a_1 \cos(2\pi f_1 t) + d(t) \\ x_2(t) &= a_2 \cos(2\pi f_2 t) + d(t) \end{aligned} \tag{2.3}$$

$$z(t) = x_1(t) - x_2(t) = a_1 \cos(2\pi f_1 t) - a_2 \cos(2\pi f_2 t) \tag{2.4}$$

Equation 2.4 can be represented as in equation 2.5. The vector $\boldsymbol{\beta}$ and the stationary linear combination $z(t)$ are called the cointegrating vector and the cointegrated residual. The cointegrated residual will continue being stationary regardless of the trend $d(t)$. It is seen that, for the two time series ($n = 2$) in equation 2.3, there is one (n - 1) linear independent cointegrating vector.

$$z(t) = \beta^T \begin{bmatrix} x_1(t) \\ x_2(t) \end{bmatrix}; \quad \boldsymbol{\beta} = \begin{bmatrix} 1 \\ -1 \end{bmatrix} \tag{2.5}$$

The following sections present the relevant mathematics required to explain the cointegration procedure applied in this thesis. These sections are based on [2], where a more detailed treatment of the cointegration technique can be found.

2.3.1 COINTEGRATION FORMULATION

In this thesis each time series is represented by a $1 \times n_o$vector, being n_o the total number of observations. The n times series are grouped into a $n \times n_o$ matrix $\mathbf{Y}$. The rows of $\mathbf{Y}$, are the individual time series represented by the $1 \times n_o$ vector $\mathbf{y}$. The columns of $\mathbf{Y}$ contains the observations of the n times series at time i and are represented by the n-vector $\mathbf{y}_i \, \forall i \in [1, \, n_o]$.

A set of two or more non-stationary time series are cointegrated if a linear combination of them is stationary. This is represented by equation 2.6, where the n-vector $\boldsymbol{\beta}$ is the cointegrating vector and $\mathbf{z}_i$ is the cointegrated residual at time i. If cointegration of the n non-stationary time series is possible, there are as many as n - 1 linear independent cointegrating vectors as is shown in the previous example with equations 2.3 to 2.5.

$$z_i = \boldsymbol{\beta}^T \mathbf{y}_i \tag{2.6}$$

A non-stationary time series $\mathbf{y}$ that becomes stationary after differencing it d times is said to be integrated of order d, which is denoted $\mathbf{y} \sim I(d)$. Thus, a time series $\mathbf{y} \sim I(0)$ is stationary. For the cointegration to be possible, the non-stationary time series must satisfy two requirements. First, they must have common trends, which is clear from equations 2.3 to 2.4. Second, they must be integrated of the same order, which means that they must have the same degree of non-stationarity. Specifically, to apply the cointegration procedure followed in this thesis, the time series must be $I(1)$, as is explained in section 2.3.3.

To evaluate the non-stationarity of a time series $\mathbf{y}$, it can be fitted to an auto-regressive model of order q (AR(q)), see equation 2.7. In this model the evolution of each observation y_i is described by its q past observations, and ε_i can be consider to be a normally distributed random noise process $\varepsilon_i \sim N(0, 1)$.

$$y_i = \sum_{j=1}^{q} a_j y_{i\text{-}j} + \varepsilon_i \tag{2.7}$$

To illustrate the non-stationarity evaluation, assume that the time series if fitted to an AR(1) model, as shown in equation 2.8. If $|a_1| < 1$ the time series will be stationary, because the $a_1 y_{i-1}$ component will decrease with time, leaving the normally distributed noise. If $|a_1| > 1$ the time series will be non-stationary and it will increase or decrease indefinitely. In the case $|a_1| = 1$ the time series will be non-stationary, but its first difference will be stationary as is shown in equation 2.9. In the latter case, the time series is said to have a unit root and it is integrated of order one such $\mathbf{y} \sim I(1)$. Then, the parameter a_1 gives information on the stationarity of a time series that is fitted to the AR(1) model.

$$y_i = a_1 y_{i\text{-}1} + \varepsilon_i \tag{2.8}$$

$$\Delta y_i = y_i - y_{i\text{-}1} = \varepsilon_i \tag{2.9}$$

In this thesis, the augmented Dickey-Fuller (ADF) test [13] is used to fit the times series to an AR(q) model in order to evaluate its non-stationarity.

2.3.2 AUGMENTED DICKEY-FULLER TEST

The ADF test follows the premise that if a time-series represented by an AR(q) model has a unit root, it will be inherently non-stationary as has been illustrated in equation 2.9. But, in the ADF test, the time series is fitted to a more sophisticated model, which is stated in equation 2.10. In this model, a suitable number q of lags are added to ensure that ε_i becomes a normally distributed random noise $\varepsilon_i \sim N(0, \sigma^2)$. The difference operator Δ is defined as $\Delta y_{i\text{-}j} = y_{i\text{-}j} - y_{i\text{-}j\text{-}1}$.

$$\Delta y_i = \rho y_{i\text{-}1} + \sum_{j=1}^{q-1} b_j \Delta y_{i\text{-}j} + \varepsilon_i \tag{2.10}$$

To fit the model, the ADF test estimates the parameters in equation 2.10 by least-square methods. Then the null hypothesis that the time series has a unit root (is a non-stationary I(1)) $H_o : \rho = 0$ is tested.

To evaluate the hypothesis, the test static t_ρ is calculated as stated in equation 2.11. There, $\widehat{\phi}$ is the least-square estimate of ϕ and σ_ϕ^2 is the variance of this parameter. The computed t_ρ is compared against a critical value t_c from Dickey-Fuller tables [13].

$$t_\rho = \frac{\widehat{\rho}}{\sigma_{\widehat{\rho}}^2} \tag{2.11}$$

The null hypothesis H_o is accepted if $t_\rho \geq t_c$, then the time series has a unit root, it is non-stationary and it is $I(1)$. If the null hypothesis H_o is rejected, the time series can be fitted to a stationary AR(q) model, then it is $I(0)$. The more negative the t_ρ obtained, the more stationary is the time series. [4]. A summary of this evaluation is presented in equation 2.12.

$$\begin{array}{lllll} t_\rho \geq t_c & \longrightarrow & Accept & H_o & \longrightarrow \quad I(1) \\ t_\rho < t_c & \longrightarrow & Reject & H_o & \longrightarrow \quad I(0) \end{array} \tag{2.12}$$

Once it has been verified that all the time series are $I(1)$, the Johansen cointegration procedure can be applied [2].

2.3.3 JOHANSEN PROCEDURE

The Johansen procedure is used to test if n non-stationary $I(1)$ time series are cointegrated. If the cointegration is possible, it gives the r linear independent cointegrating vectors $(r < n)$, and determines which of these cointegrating vectors yields the most stationary cointegrated residual. The implicit assumption of this procedure is that all the non-stationary time series being tested are $I(1)$.

The AR(q) model in equation 2.7 can be extended to include n time series. Doing this, the vector auto-regressive model VAR(k), in equation 2.13, is obtained. In this model the evolution of the n time series is described by combinations of k past outputs from each series. The n-vector $\mathbf{y}_i$ contains the observations of the n time series at time i $\forall i \in [1, n_o]$. The $n \times n$

matrix $\mathbf{A}_i$ contains the parameters of the model and the components ε_i of the n-vector $\boldsymbol{\varepsilon}_i$ can be considered to be generated from normally distributed random noise process $\varepsilon_i \sim N(0, 1)$.

$$\mathbf{y}_i = \sum_{j=1}^{k} \mathbf{A}_j \mathbf{y}_{i\text{-}j} + \boldsymbol{\varepsilon}_i \tag{2.13}$$

To test the cointegration of the time series, the Johansen procedure transforms the VAR(k) model, equation 2.13, into the vector error-correction model (VECM) stated in equation 2.14. In this model, k is the model order or number of included lags. The n-vector $\boldsymbol{\varepsilon}_i$ is a normally distributed noise $\boldsymbol{\varepsilon}_i \sim N(0, \mathbf{S})$. The $n \times n$ matrices $\boldsymbol{\Pi}$ and $\mathbf{C}_j$ are parameter matrices.

$$\Delta \mathbf{y}_i = \boldsymbol{\Pi} \mathbf{y}_{i\text{-}1} + \sum_{j=1}^{k-1} \mathbf{C}_j \Delta \mathbf{y}_{i\text{-}j} + \boldsymbol{\varepsilon}_i \tag{2.14}$$

The consideration that the time series are $I(1)$ implies that $\Delta \mathbf{y}_i$ and $\Delta \mathbf{y}_{i\text{-}j}$ are stationary. Then, if a true VECM(k) exists, the series given by $\boldsymbol{\Pi} \mathbf{y}_{i-1}$ would be stationary and the time series would be cointegrated. In that case, since $\mathbf{y}_{i\text{-}1}$ is of dimension n, there must be at most $n-1$ linear independent combinations of this product, or in other works the parameter matrix $\boldsymbol{\Pi}$ must be rank deficient, say of rank r ($r < n$). Therefore $\boldsymbol{\Pi}$ can be decomposed into two $n \times r$ matrices as stated in equation 2.15.

$$\boldsymbol{\Pi} = \mathbf{A}\mathbf{B}^T \tag{2.15}$$

If a true VECM(k) exists, the rows of $\boldsymbol{\Pi}$ give the linear combination that makes $\mathbf{y}_{i-1}$ linear. Each row of $\boldsymbol{\Pi}$ is a linear combination of the rows of $\mathbf{B}^T$, then the rows of $\mathbf{B}^T$ are the cointegrating vectors [10]. In other words, each of the r columns of $\mathbf{B}$ can be taken as one cointegrating vector $\boldsymbol{\beta}$.

In a true VECM(k), the parameters in $\boldsymbol{\Pi}$ contain information about the long-run equilibrium between the time series, see equation 2.14. The parameters in $\mathbf{C}_j$ account for the short-run adjustments needed to return $\Delta \mathbf{y}_i$ to equilibrium after changes. In equation 2.15, the parameters in $\mathbf{B}$ are the long-run equilibrium coefficients. The parameters in $\mathbf{A}$ represent the speed of adjustment to disequilibrium [18].

In the Johansen procedure, for a selected lag value k, the maximum likelihood estimates of the parameters $\mathbf{C}_j$ and $\mathbf{A}$ are expressed in terms of $\mathbf{B}^T$. Then $\boldsymbol{\varepsilon}_i$, in equation 2.14, is expressed in function of $\mathbf{B}^T$. The estimate $\mathbf{B}^T$ is $\hat{\mathbf{B}}^T$. It is computed solving the eigenvalue problem that maximize the likelihood of observing the entire correct sequence of $\boldsymbol{\varepsilon}_i$. This likelihood is equal to $\prod_{i=1}^{n_o} p(\boldsymbol{\varepsilon}_i)$, where $p(\boldsymbol{\varepsilon}_i)$ is the probability density function of $\boldsymbol{\varepsilon}_i$. The computed eigenvectors are the columns of $\hat{\mathbf{B}}^T$. It turns out that the best cointegrated combination $\hat{\mathbf{B}}^T \mathbf{y}_{i\text{-}1}$ is given by the eigenvector associated with the largest eigenvalue. The larger the eigenvalue, the more stationary the cointegrated combination. Then the eigenvector related to the largest eigenvalue is chosen as the cointegrating vector $\boldsymbol{\beta}$.

In the previous steps, to find $\hat{\mathbf{B}}^T$, it is assumed that a true VECM(k) exists for the times

series. After calculating $\hat{\mathbf{B}}^T$ and finding out $\boldsymbol{\beta}$, the Johansen procedure performs a statistical test to verify if the time series are cointegrated with the selected number of lags k. In this test, the rank r of $\boldsymbol{\Pi}$ is computed to verify that $0 < r < n$. If $r = 0$, cointegration of the time series is not possible with this procedure for the selected k. If $r = n$, full rank, cointegration is not possible with this procedure for the selected p, and the inference is that the time series are stationary($I(0)$). If $0 < r < n$, a true VECM(k) exists, r cointegrating vectors are found, and the one related to the largest eigenvalue is chosen to be used as $\boldsymbol{\beta}$.

After obtaining $\boldsymbol{\beta}$, the time series are projected onto $\boldsymbol{\beta}$ to compute the stationary cointegrated residual $\mathbf{z}$ applying equation 2.16. The $n \times n_o$ matrix $\mathbf{Y}$ contains the n times series and $\mathbf{z}$ is a $1 \times n_o$ vector.

$$\mathbf{z} = \boldsymbol{\beta}^T \mathbf{Y} \tag{2.16}$$

In case one or more stationary time series $I(0)$ are input into the Johansen procedure it gives trivial solutions, with cointegrating vectors that contain ones and zeros related to the stationary and non-stationary inputs respectively. The zero components remove the information of the non-stationary signals from the residual. This is another reason to check the non-stationarity of the time series before testing for cointegration.

The cointegrating vectors obtained from the Johansen procedure could be real or complex values, even if the input time series are real $\mathbf{Y} \in \mathbb{R}^{n \times n_o}$. In this thesis, only the real cointegrating vectors $\boldsymbol{\beta} \in \mathbb{R}^n$ are taken into account for the damage detection procedure described in the following section.

2.3.4 COINTEGRATION FOR STRUCTURAL DAMAGE DETECTION

For SDD damage detection, cointegration is used to removed or at least mitigate the influence of the common EOV trends in the response signals. The cointegrated residual can be used as a metric for outlier analysis. The aim is to represent the different states of the structure with cointegrated residuals that are independent of the EOVs, but still sensitive to damage.

OUTLIER ANALYSIS WITH COINTEGRATED RESIDUALS

For the outlier analysis, the baseline model is constructed with a training cointegrated residual obtained from the reference state of the structure. To this end, the training features $\mathbf{X}_{tr} \in \mathbb{R}^{p \times n_{tr}}$ computed from a set of n_{tr} training observations are used as the time series $\mathbf{Y}$ in the Johansen procedure. From this procedure, the cointegrating vector $\boldsymbol{\beta} \in \mathbb{R}^p$ is calculated. Then, the training cointegrated residual $\mathbf{z}_{tr} \in \mathbb{R}^{1 \times n_{tr}}$ is obtained from equation 2.16.

If such cointegrating vector $\boldsymbol{\beta}$ can be found, the stationarity or non-stationarity of the features from the testing state projected onto $\boldsymbol{\beta}$ can be used as an indicator that the structure continues to operate in its reference state or not. The appearance of a new trend due to damage will usually destroy the balance imposed by the cointegrating vector and leave the damage exposed [1].

To find $\boldsymbol{\beta}$, a suitable set of damage-sensitive and cointegrable training features $\mathbf{X}_{tr}$ are needed. There are two requirements that must be fulfilled. First, these features must share the EOVs' trend. In SDD, response signals from the same structure, and the features computed from them, are likely to share common trends if they are driven by the same EOVs. Second, the features must be $I(1)$ to apply the Johansen procedure. Many of the response signals of interest to SDD, and the features computed from them, appear to exhibit non-stationarity[1]. However, to avoid null or full rank solutions of $\boldsymbol{\Pi}$ in equation 2.15, the features are tested with the ADF test to ensure that they are $I(1)$.

Since the cointegrated residual is distributed around its mean, it could give positive or negative values. For this reason, the threshold is defined with an upper and lower limit. These limits establish lower and upper boundaries for $\mathbf{z}_{tr}$ according to a false positive allowance. Each of the limits leaves half of the allowed false positives outside their boundaries.

The state of the structure to be evaluated is represented by a set of n_{te} testing observations. From these observations, the testing features $\mathbf{X}_{te} \in \mathbb{R}^{p \times n_{te}}$ are calculated. Then, the testing cointegrated residual $\mathbf{z}_{te} \in \mathbb{R}^{1 \times n_{te}}$ is computed with equation 2.16. In that computation, the cointegrating vector $\boldsymbol{\beta}$ obtained from $\mathbf{X}_{tr}$ is used. The computed $\mathbf{z}_{te}$ is plotted and evaluated against the threshold. Figure 2.7 is a representation of outlier analysis using a cointegrated residual as a metric.

PERFORMANCE INDICATORS

The performance indicators FPR, TPR and AUC are computed, taking into consideration both threshold limits and following the procedure described in section 2.1.1. The test statistic t_ρ, computed from the ADF test of $\mathbf{z}_{tr}$ is added as indicator, equation 2.11. With this indicator, the stationarity of $\mathbf{z}_{tr}$ is evaluated.

SELECTION OF LAG VALUES

The number of lags q to be included in the ADF test moed, equation 2.10, depends on the characteristic of the feature being tested, . To this author's knowledge, the literature does not offer a general rule or recommendation for q in SDD applications. In this thesis, the ADF test is used in two cases. First, to check the stationarity or non-stationarity of the features to avoid useless attempts of cointegration. Second, to assess the stationarity of the cointegrated residuals for comparison. In both cases, since the goal is not forecasting the features, we are not particular interested in the parameters of the ADF test model, equation 2.10. For this reason, the number of lags for the ADF test is set as half the maximum value given by equation 2.17, $q = k_{max}/2$, and reduced or increased if it is allowed or required.

The Johansen procedure requires selection of the number of lags k to be included in the VECM, equation 2.14. The selection of k is one of the most important issues for the implementation of this procedure. The results of the Johansen procedure, the cointegrating vector and the cointegrated residual, relies on a proper selection of k. A small k may not

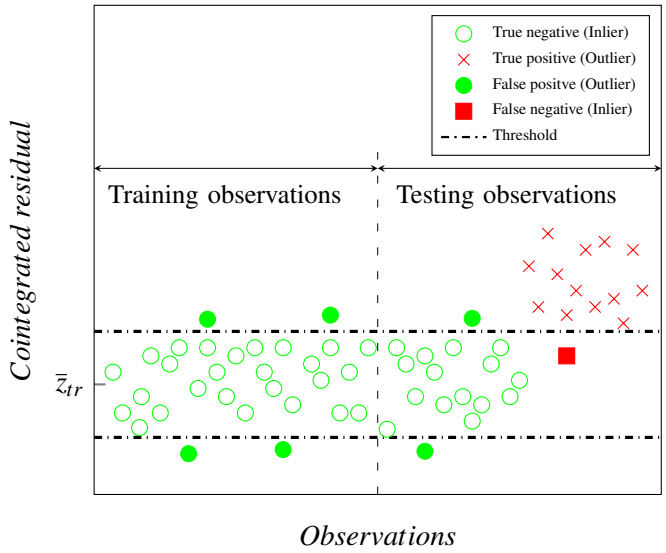

Figure 2.7: Representation of outlier analysis with cointegrated residuals. The threshold is based on false positive allowance of training observations.

capture the dynamic behaviour of the features. A large value will distort the data by adding unnecessary lag terms and lead to a decrease in the power of the cointegration test [4]. Different criteria and rules of thumb for the selection of k are summarized in [4]. There, a range of values $k \in [k_{min},\, k_{max}]$ to test for cointegration is proposed. This range is stated in equation 2.17, where the square brackets denote the integer part of the result. In this thesis, that range is used as a starting point to find the cointegrating vector.

$$\begin{aligned} k_{min} &= 3 \\ k_{max} &= \left[12\left(\tfrac{n_{tr}}{100}\right)^{1/4}\right] \end{aligned} \tag{2.17}$$

SELECTION OF THE COINTEGRATING VECTOR

For each k value, the Johansen procedure may compute as many as $n-1$ linearly independent cointegrating vectors. That gives a maximum of $(n-1)\times(k_{max}-k_{min}+1)$ possible cointegrating vectors. The most feasible for outlier analysis needs to be selected from them. In this thesis, two options are proposed to perform that selection, Lag Option 1 and Lag Option 2, which are presented below. The evaluation of the effectiveness of the obtained cointegrating vectors for outlier analysis is based on the performance indicators (t_ρ, FPR, TPR and AUC). The selected $\boldsymbol{\beta}$ should yield cointegrated residuals that stay within the threshold limits when the structure operates in its reference state, and outside the limits if not.

Lag Option 1 The procedure is as follows. First, perform the cointegration test for each $k \in [k_{min},\, k_{max}]$, equation 2.17. In each test, where the cointegration is possible, select the

cointegrating vector related to the largest eigenvalue. This is in agreement with the Johansen procedure and gives a maximum of $(k_{max} - k_{min} + 1)$ cointegrating vectors. Second, compute the cointegrated residuals for the selected cointegrating vectors. Third, perform the ADF test for each cointegrated residual and compute their t_ρ, equation 2.11. The tests are performed with the same q. Fourth, select as the cointegrating vector, the one that gives the cointegrated residual with the lowest t_ρ (most stationary).

Lag Option 2 According to the Johansen procedure, subsection 2.3.3, for a specific k, the cointegrating vector related to the largest eigenvalue is the one that gives the most stationary cointegrated residual. However, if the cointegrated residuals are tested for stationarity with the ADF test, the most stationary one is not always related to the largest eigenvalue. It is because the Johansen procedure and the ADF test are based on different statistical procedures. Taking that into account, Lag Option 2 is conducted as follows. First, compute all of the feasible cointegrating vectors performing the Johansen procedure for each $k \in [k_{min},\, k_{max}]$. This gives a maximum of $(n-1) \times (k_{max} - k_{min} + 1)$ cointegrating vectors. Second, compute their cointegrated residuals. Third, test all cointegrated residuals for stationary with the ADF test and compute their t_ρ, equation 2.11. The tests are performed with the same q. Fourth, select as the cointegrating vector, the one that gives the cointegrated residual with the lowest t_ρ (most stationary).

SUMMARY OF THE PROCEDURE TO OBTAIN AND EVALUATE $\boldsymbol{\beta}$

The procedure to obtain $\boldsymbol{\beta}$ and to evaluate its performance for outlier analysis is:

- Step 1: Select a damage-sensitive feature of dimension p.
- Step 2: Store the features associate with the n_{tr} training observations in a matrix $\mathbf{X}_{tr} \in \mathbb{R}^{p \times n_{tr}}$.
- Step 3: Verify that each row of $\mathbf{X}_{tr}$ is $I(1)$ with the ADF test. Use a lag value $q = k_{max}/2$ as starting point. Continue if the series are found to be $I(1)$. If not, another feature or approach is required (Step 1).
- Step 4: Compute the range of lag values to be used for the Johansen procedure $k \in [k_{min},\, k_{max}]$, equation 2.17.
- Step 5: Obtain one feasible $\boldsymbol{\beta}$ from Lag Option 1.
- Step 6: Obtain another feasible $\boldsymbol{\beta}$ from Lag Option 2.
- Step 7: Compute $\mathbf{z}_{tr}$ and $\mathbf{z}_{te}$ from the $\boldsymbol{\beta}$s obtained with Lag Option 1 and Lag Option 2, use equation 2.16.
- Step 8: Define the threshold. Plot $\mathbf{z}_{tr}$ and $\mathbf{z}_{te}$ of each option with the threshold limits.
- Step 9: Compute the performance indicators (t_ρ, FPR, TPR and AUC).
- Step 10: Evaluate the performance indicators and the plots in order to assess the effectiveness of the $\boldsymbol{\beta}$s computed from both options. A good $\boldsymbol{\beta}$ should give results that identify damage (TPR) without or minimum quantity of false positives (FPR).

Also, evaluate if $\mathbf{z}_{te}$ remain stable between the thresholds limits. AUC is used to asses the whole performance of each option, and t_ρ is used to assess the stationarity of $\mathbf{z}_{tr}$.

- Step 10: If a feasible $\boldsymbol{\beta}$ is not found, search with bigger values of k. Repeat steps 1 to 10 for $k \in [k_{max}+1,\ k_{max}+10]$.

In steps 5 and 6, it is assumed that at least one cointegrating vector is found with the Johansen procedure.

Chapter 3

NUMERICAL APPLICATIONS

To to get more insight into their applications and assumptions, and to validate their utility for vibration-based SDD, the methods outlined in chapter 2 are tested with numerical examples before applying them to experimental data. The numerical simulations are based on the spring-mass-damper system with $n = 10$ degrees of freedom (DOF) depicted in figure 3.1.

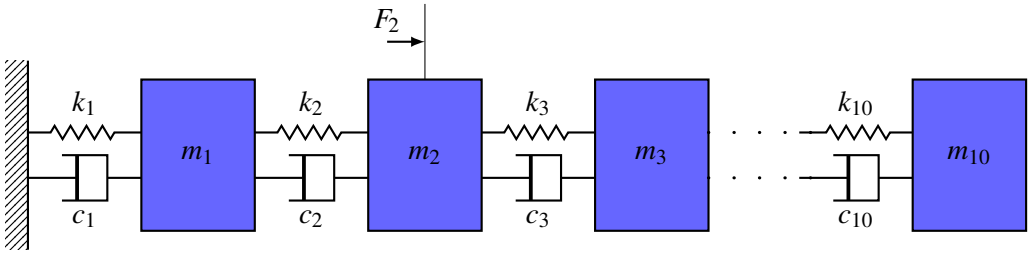

Figure 3.1: Spring-mass-damper system with ten DOF.

One end of the system is fixed and a driving force is applied to the second mass. The mass m_i and stiffness k_i are set constant over time. A modal damping ratio is defined to model the viscous damping as modal damping.

Damage is introduced by decreasing the stiffness of the third spring of the system k_3 up to 30%. This generates undamped eigenfrequencies of the system below 11 Hz for all the simulated cases. With this in mind, a cosine swept with frequency increasing linearly from 0 to 20 Hz is set as the driving force, see figure 3.2. It will excite all modes in the system.

The nominal displacement responses to the driving force at each DOF, $\mathbf{y} \in \mathbb{R}^{1\times n_t}$, with n_t sample points, are computed through Newmark integration for 20 seconds at a sampling frequency $f_s = 60Hz$. Results for all the DOF are stored in a nominal displacement response matrix $\mathbf{Y} \in \mathbb{R}^{n\times n_t}$. Figure 3.3 shows the nominal displacement response at the fourth DOF.

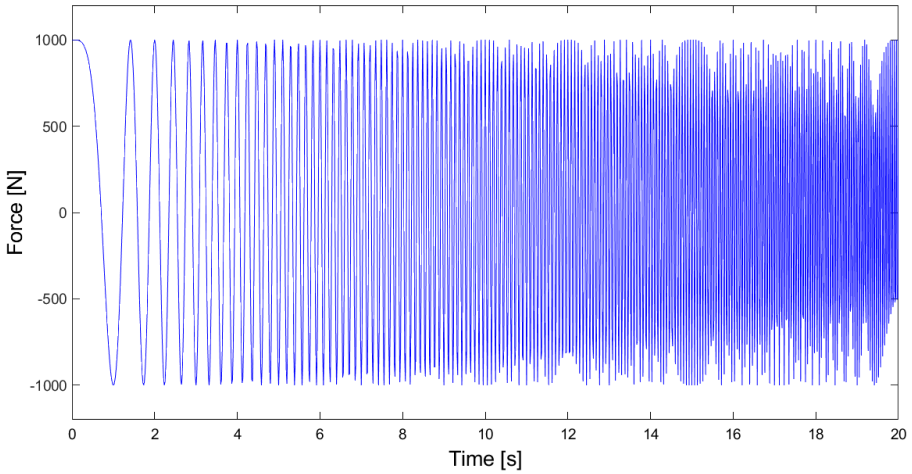

Figure 3.2: Linear sweep-frequency cosine driving force with frequency range 0 - 20 Hz.

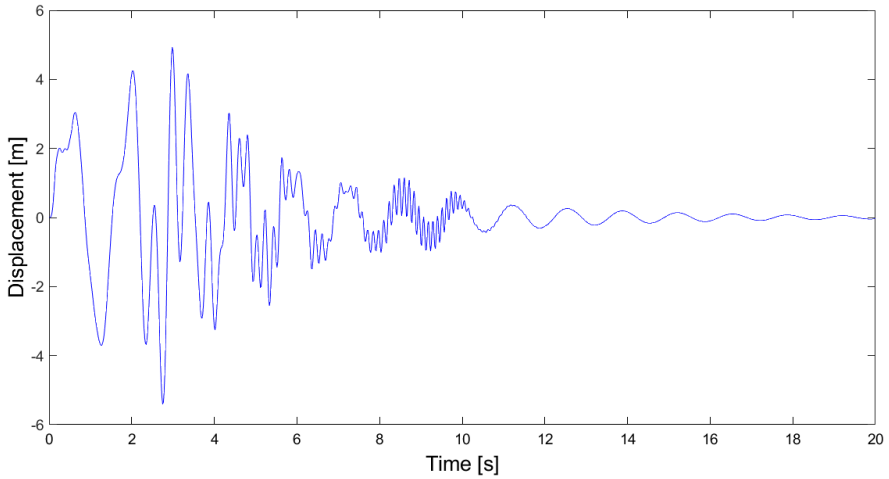

Figure 3.3: Nominal displacement response in the fourth DOF.

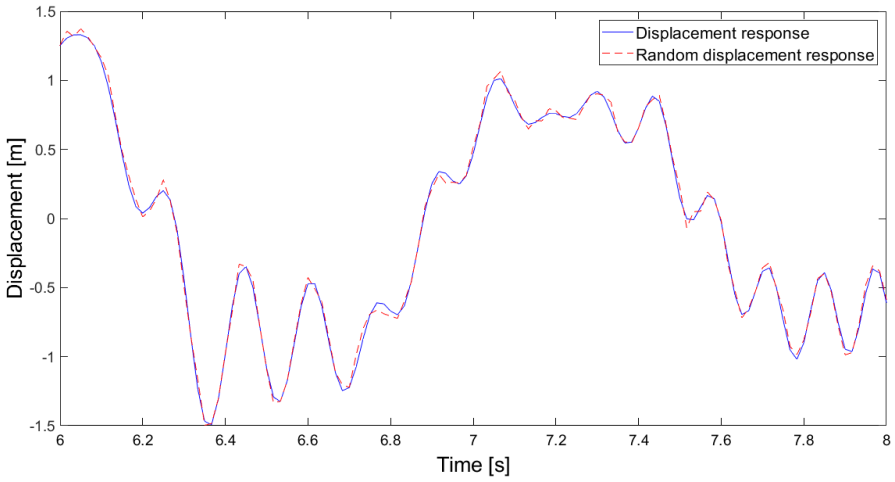

Figure 3.4: displacement response compared with the nominal displacement response at the fourth DOF.

Random normally distributed noise is added to the nominal displacement responses to represent instrumental noise. This also generates random observations to represented the states of the system. The added noise has zero mean and standard deviation equal to 1% of the standard deviation of each nominal displacement response. Figure 3.4 shows an example of one of these displacement responses compared against the nominal displacement response for the fourth DOF.

Four states of the system are defined with the random observations. First, the training state that corresponds to the undamaged system, and is represented by n_{tr} random training observations. Second, the testing undamaged state that also corresponds to the undamaged system, and is represented by n_{te} random testing undamaged observations. The last two are the testing damaged state 1 and testing damaged state 2, which correspond to the damage system with different levels of damage. They are represented by n_{d1} and n_{d2} random testing damaged observations.

3.1 OUTLIER ANALYSIS APPLICATIONS

3.1.1 SIMULATED CASE 1: SCENARIO WITHOUT EOVs

To construct the baseline model, $n_{tr} = 200$ random training observations are generated from the displacement responses of the undamaged state of the system. In a similar way, $n_{te} = 100$ random testing observations are computed from the undamaged system. They will be used to test the ability of the approach to recognize the healthy state during testing.

The damaged states are simulated by reducing abruptly the stiffness of the third spring of the system. The mentioned stiffness is reduced by 20% for damaged state 1 and 30% for damaged state 2. For each damaged state $n_{d1} = n_{d2} = 100$ random testing damaged observa-

tions are computed.

The feature selected for this example is a vector that contains the unique elements of the covariance matrix $\mathbf{S} \in \mathbb{R}^{n \times n}$ between the n displacement responses at each observation. It means that the healthy state of the system is represented for the relations between its displacements responses due to the driving force. Any variation in these relations that produce a metric bigger than the threshold will classify the current state of the system as damaged.

The unique elements of the covariance matrix $\mathbf{S}$ are computed for each observation by equation 3.1, where μ is the mean of each response given by equation 3.2. The unique elements are stored in the feature vector $\mathbf{x} \in \mathbb{R}^p$. The dimension of the feature vector p, number of unique elements, is given by equation 3.3. The feature vectors for n_o observations are stored in the feature matrix $\mathbf{X} \in \mathbb{R}^{p \times n_o}$. In this example, $n = 10$ gives $p = 55$.

$$\forall i \leq j \in [1,\, n]: \quad \mathbf{S}_{ij} = \frac{1}{n_t - 1} \sum_{k=1}^{n_t} (\mathbf{Y}_{ik} - \mu_i)(\mathbf{Y}_{jk} - \mu_j) \tag{3.1}$$

$$\forall i \in [1,\, n]: \quad \mu_i = \frac{1}{n_t} \sum_{k=1}^{n_t} \mathbf{Y}_{ik} \tag{3.2}$$

$$p = \frac{n(n+1)}{2} \tag{3.3}$$

Applying this procedure, the training feature matrix $\mathbf{X}_{tr} \in \mathbb{R}^{p \times n_{tr}}$, the testing undamaged feature matrix $\mathbf{X}_{te} \in \mathbb{R}^{p \times n_{te}}$, the testing damaged 1 feature matrix $\mathbf{X}_{d1} \in \mathbb{R}^{p \times n_{d1}}$ and the testing damaged 2 feature matrix $\mathbf{X}_{d2} \in \mathbb{R}^{p \times n_{d2}}$ are computed from the corresponding observations.

The baseline model is constructed with mean $\bar{\mathbf{x}} \in \mathbb{R}^p$ and covariance matrix $\mathbf{S} \in \mathbb{R}^{p \times p}$ from the training features stored in $\mathbf{X}_{tr}$. Based on this model, the Mahalanobis square distances are calculated, as exclusive values, for the training, testing undamaged and the two testing damaged sets of features applying equation (2.2). The threshold value is set as the value that allows 1% of false positives in the training data.

Figure 3.5 shows the results. It shows the training observations in black color, the testing undamaged observations in blue color, the testing damaged 1 observations in green color, and the testing damaged 2 observations in red color. It is clear that the selected feature and the Mahalanobis squared distances allow to classify the undamaged and damaged states. Three false positives are observed in the testing undamaged data, and all testing damaged observations are correctly classified. With the current threshold, the FPR is equal to 3% and TPR is equal to 100%.

The ROC curve from all testing observations is plotted in Figure 3.6. In this case, the AUC equals to one, and the damaged classification is perfect for any selected threshold.

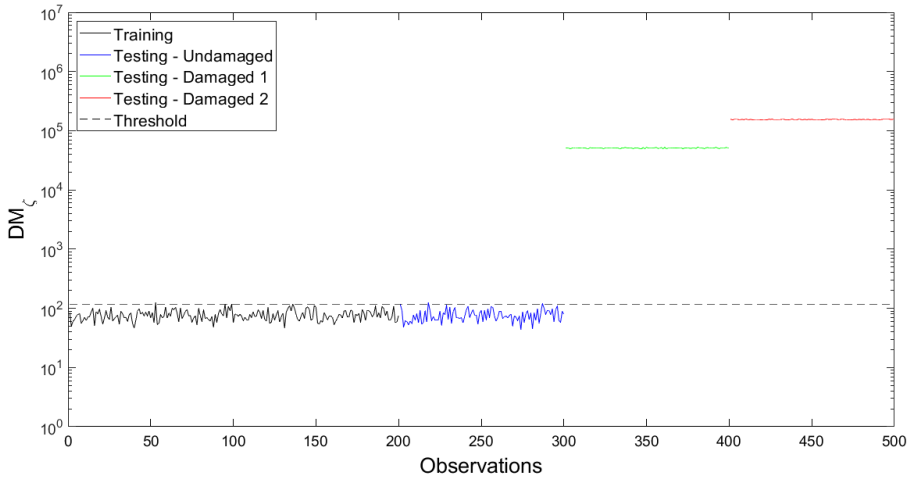

Figure 3.5: Mahalanobis square distances for the damage detection approach of a spring-mass-damper system without EOVs, using unique elements of the covariance matrix between displacement responses as a feature.

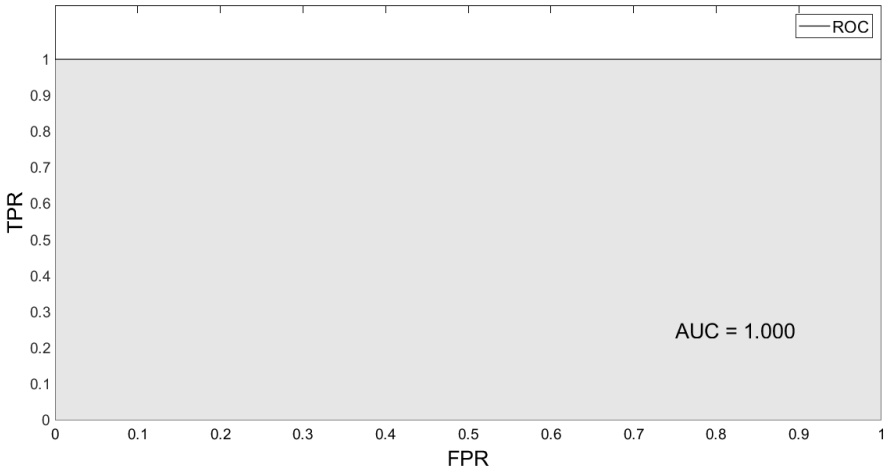

Figure 3.6: ROC for the damage detection approach of a spring-mass-damper system without EOVs, using unique elements of the covariance matrix between displacement responses as a feature and Mahalanobis square distances as metric.

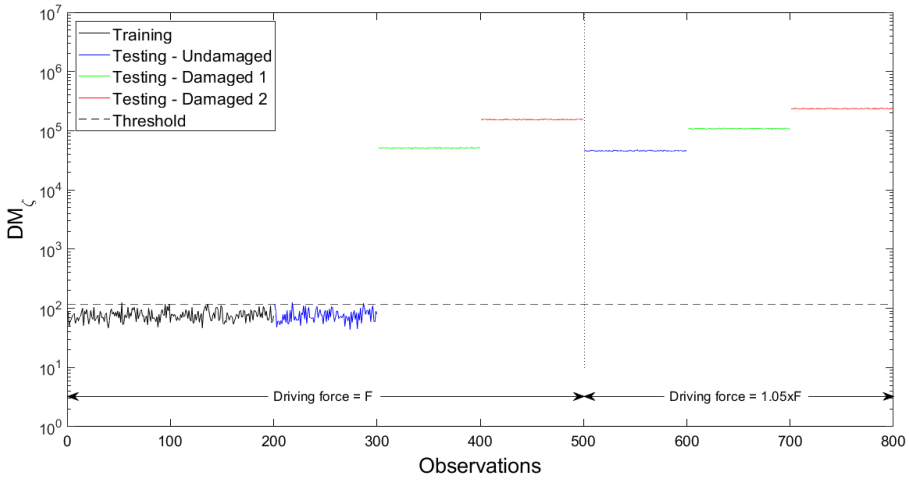

Figure 3.7: Mahalanobis square distances for the damage detection approach of a spring-mass-damper system with driving force amplitude variation of 5%, using unique elements of the covariance matrix between displacement responses as a feature.

3.1.2 SIMULATED CASE 2: SCENARIO WITH OVs

To investigate the sensitivity of the selected feature to EOVs, a loading variation is introduced. Three new sets of testing observations are generated from the displacement responses due to a driving force with an increase in amplitude of 5%. The testing undamaged and damage features are computed, and its Mahalanobis squares distances are calculated with the same baseline model used for the first simulated case (same training features). Figure 3.7 shows the results in comparison with the previous results without EOVs. The approach recognises the two damaged states with force variability. However it fails to correctly classify any of the testing undamaged observations, which results in a FPR of 100%.

For the results in figure 3.7, it is clear that the selected feature is highly sensitive to loading variations, and an extra step to mitigate the influence of the force variation in the results is required. To mitigate this influence, the current feature is normalized by its standard deviations σ [20]. The normalized feature is computed by equation 3.4. The standard deviation σ is calculated from equations 3.5 and 3.2.

$$\forall i \leq j \in [1,\, n]: \quad \frac{\mathbf{S}_{ij}}{\sigma_i \sigma_j} \tag{3.4}$$

$$\forall i \in [1,\, n]: \quad \sigma_i = \frac{1}{n_t - 1} \sqrt{\sum_{k=1}^{n_t} (\mathbf{Y}_{ik} - \mu_i)^2} \tag{3.5}$$

A new baseline model is computed from the training normalized features, and the Mahalanobis square distances are calculated for the training and testing normalized features for

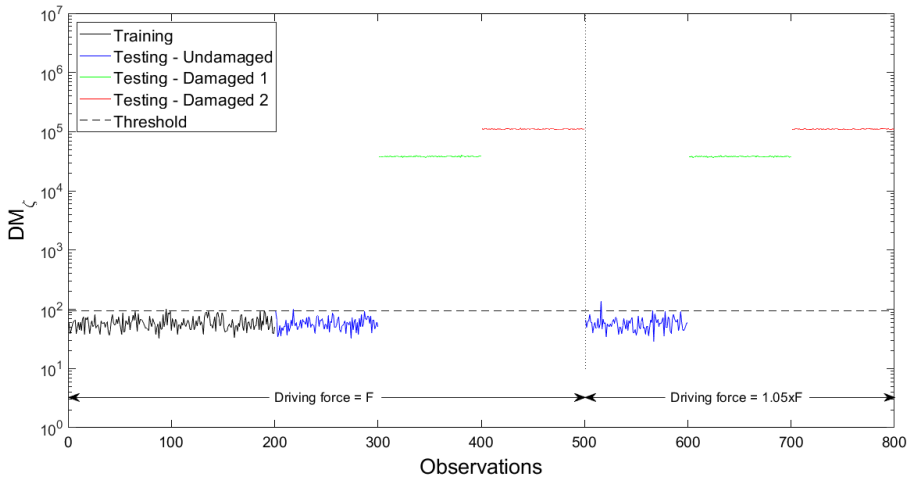

Figure 3.8: Mahalanobis square distances for the damage detection approach of a spring-mass-damper system with driving force amplitude variation of 5%, using unique elements of the covariance matrix between displacement responses normalized by its standard deviations as a feature.

both force scenarios. Figure 3.8 presents the results. Despite the force variation, only FPR $= 5\%$ is obtained from the testing undamaged observations, and all testing damaged observations are correctly classified. The results show that the normalized feature is insensitive to the amplitude force variation.

It is important to note that the normalized feature works, in this case, because normalizing the covariance matrix components with respect to their standard deviations gives the correlation coefficients among the responses, and these are independent of the force amplitude for this linear system. In the next case, a more complicated case of EOVs is investigated.

3.1.3 SIMULATED CASE 3: SCENARIO WITH EVs

In the previous cases, it was assumed that the stiffness of the springs are not a function of time or temperature. The present case study introduces a time-dependent stiffness as a function of temperature, where the temperature at each spring follow a defined temperature field among observations. This allows to investigate the influence of temperature variation in the damage detection approach.

Temperature fields are defined for each spring in the system. The temperature varies in space among the springs and in time among the observations, while it is assumed to be constant during the time the n_t samples are measured at each observation. In space, the temperature at each spring decreases 0.5°C from the first spring (fixed end) towards the last spring (free end). In time, among the observations of each state, temperatures $T_i \; \forall i \in [1, \, n_o]$ are characterized for non-stationary random walk models [10] as given by equation 3.6, where $\varepsilon_i \sim N(0, \, 1)$ is a normally distributed random noise.

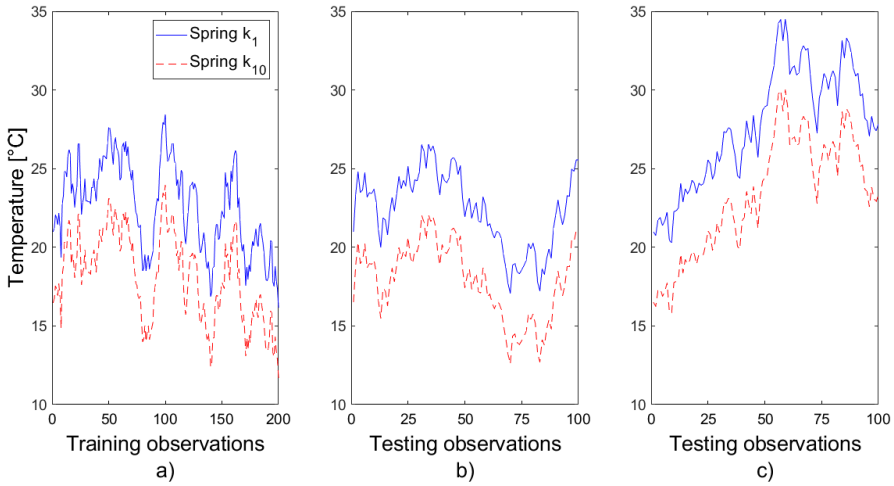

Figure 3.9: Temperature fields over observations. For visualization purpose only temperatures for springs one and ten are shown (temperatures for other springs lie between them). Figure a), temperature field for training observations. Figure b), temperature field for testing observations with temperatures inside the range of temperatures of training observations, Figure c) temperature fields for testing observations with temperatures outside the range of temperatures of training observations

$$T_i = T_{i-1} + \varepsilon_i \tag{3.6}$$

From the spatial and time distributions, three temperature fields are defined for each spring; one for the training observations and two for the testing observations. Figure 3.9 shows the three temperature fields at springs number one and ten. Temperature fields at other springs lie between them; these are not shown for visualization purposes. The temperature fields give the temperature of each spring at any observation. Temperatures in figure 3.9b) are inside the range of temperatures of the training observations, see figure 3.9a). Temperature fields in figure 3.9c) give temperatures outside the range of temperatures of the training observations; these will be used to simulate the effects of abnormal temperatures in the testing observations.

The stiffness as a function of the temperature is defined as a decreasing linear function, see figure 3.10. The stiffness of each spring $k_i \forall i \in [1,\ 10]$ at a particular observation is obtained from this function according to the temperature of each spring at that particular observation.

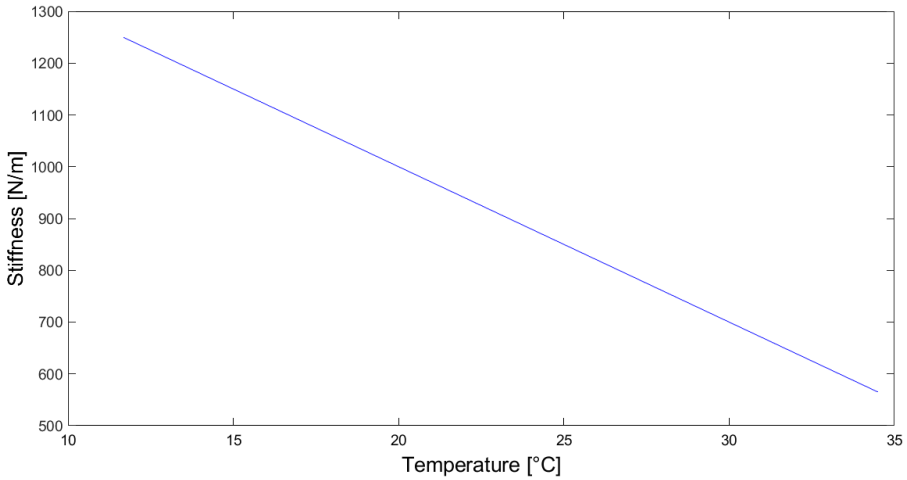

Figure 3.10: Stiffness as a function of temperature

The system stiffness matrix is calculated at each observation according to the temperature field. Then nominal displacements responses are computed for the linear system thorough Newmark integration. Random normally distributed noise is added to the nominal displacement responses to represent instrumental noise. As in the previous case studies, the added noise has zero mean and standard deviation equal to 1% of the standard deviation of each displacement response.

Features and Mahalanobis square distances are obtained by equations 3.1 and 2.2 respectively. The features generated for each state are graphically verified to not deviate from the normal distribution.

Figure 3.11 shows the results when temperatures for the testing observations are obtained from the temperature fields shown in figure 3.9b), which are in the same range as temperatures for the training observations, in other words, when all temperature variations in testing phase were taken into account in the training phase. In the bottom, the average temperature from the ten springs at each observation is displayed.

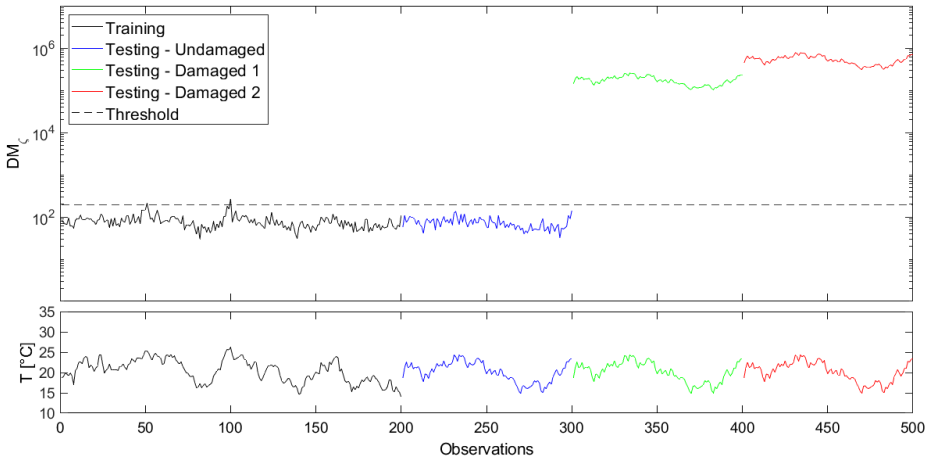

Figure 3.11: Mahalanobis square distances without abnormal temperatures in the testing observations. In the bottom the average temperature of the ten springs at each observation is displayed.

Testing undamaged and testing damaged observations are correctly classified since the whole temperature variability is accounted for during the training phase [21]. However, in a real case, it will not be possible to consider all EOVs during the training phase.

To investigate the influence of temperature variations in the testing phase that are not taken into account in the training phase, a new simulation is conducted. In this case, temperatures for the testing observations are obtained from the temperature fields show in figure 3.9c), where the temperature range is different than the range for the training observations. Results are depicted in figure 3.12.

Testing damaged observations are correctly classified; however, 42% of the testing undamaged observations are incorrectly classified as damaged. It is due to the abnormal temperature variations which produce discordances in the features, with respect to the baseline model, higher than the allowed threshold.

The Mahalanobis square distances from the undamaged testing observations with abnormal temperatures show a similar tendency as the temperature over the observations. It means that the features are highly sensitive to the temperature variation outside the training range, which is explained because the variation of stiffness, due to the abnormal temperatures, increases the discordance with respect to the baseline model.

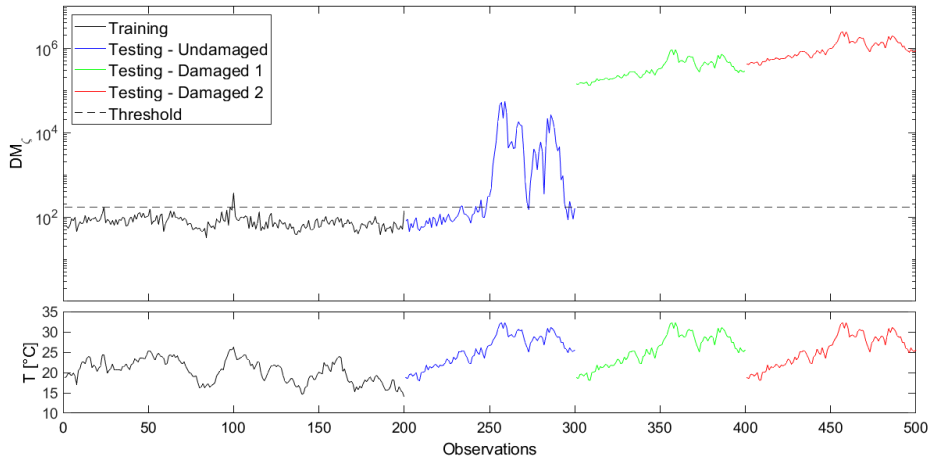

Figure 3.12: Mahalanobis square distances with abnormal temperatures in the testing observations. In the bottom the average temperature of the ten springs at each observation is displayed.

A new simulation is conducted to investigate if the normalized feature, equation 3.4, computed from the same responses can mitigate the influence of these abnormal temperature variations as in the case of amplitude force variation, figure 3.8. Results are shown in figure 3.13. Both testing damaged states are correctly classify; however, the testing undamaged state has a FPR equal to 42% as in the previous simulation. Even with normalized features, the presence of abnormal temperatures, that have not been taken into account in the training phase, produces enough discordance to incorrectly classify almost one-half of the undamaged testing observations, making the approach unreliable for this case.

3.1.4 SIMULATED CASE 4: SCENARIO WITH EVs

In the last case study, the use of a modal parameter as feature is examined. To this purpose, the feature vector is constructed with the ten undamped eigenfrequencies of the system ω_n. At each observation, the stiffness matrix of the system is computed according to the temperature fields. Then, the ten ω_n are computed solving the eigenvalue problem [11]. Normal distributed noise with 1% standard deviation is added to account for instrument noise. After that, the corresponding Mahalanobis square distances are calculated.

The results are shown in figure 3.14. Due to the abnormal temperatures, the metric is unable to classify all the testing undamaged observations as undamaged. The FPR is equal to 26%. For this simulated case study, the Mahalanobis squares distances from ω_n show less sensitivity to the temperature variations. However, in practical applications of SDD, the use of modal parameters as feature is not feasible since they are more sensitive to EOVs than damage [17, 21]. In this thesis, ω_n is used as feature with a didactic purpose.

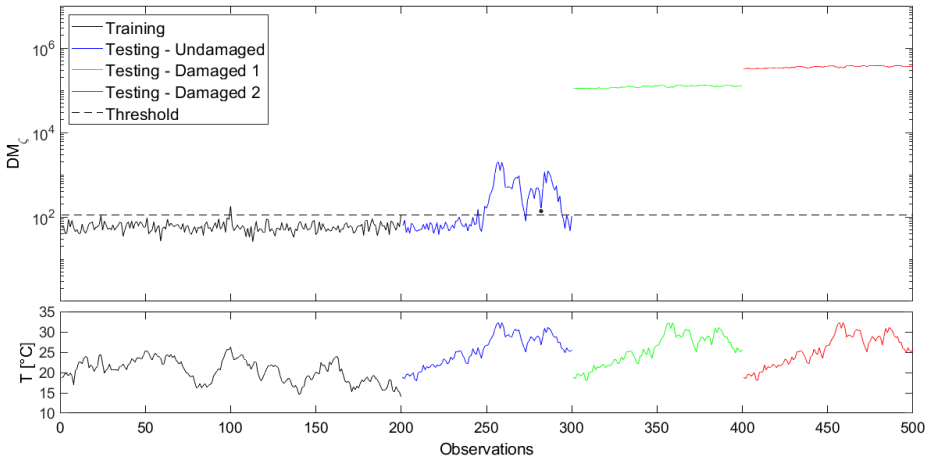

Figure 3.13: Mahalanobis square distances from normalized features, and with abnormal temperatures in the testing observations. In the bottom the average temperature of the ten springs at each observation is displayed.

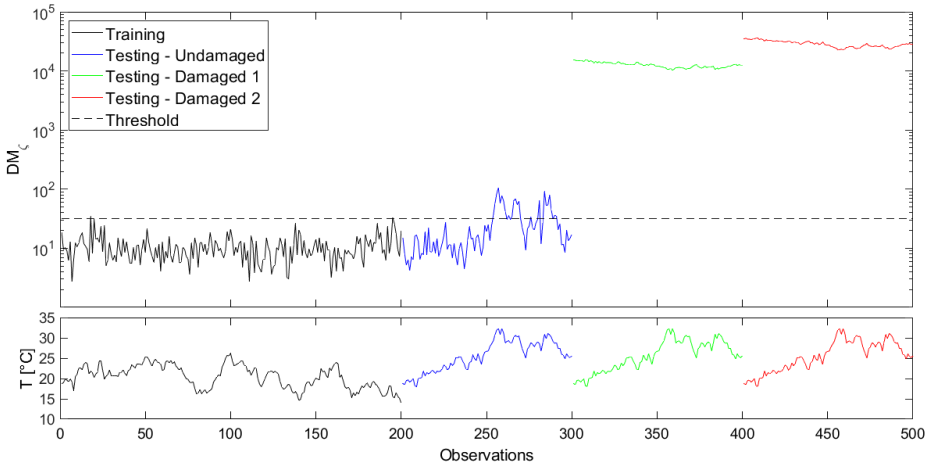

Figure 3.14: Mahalanobis square distances from Wn as feature, and with abnormal temperatures in the testing observations. In the bottom the average temperature of the ten springs at each observation is displayed.

3.1.5 SUMMARY OF SIMULATION STUDIES

From the simulated cases, it is clear that the selection of a feature that is sensitive to damage but insensitive to EOVs, or a more robust approach to mitigate the EOVs' influence in the results is required. The selection of such feature is not straightforward. However, different approaches exist that can project out the EOV-sensitive component of the features while preserving the damage sensitivity [23]. One approach that can remove the EOVs' influence in the measured responses or features is cointegration.

3.2 COINTEGRATION APPLICATIONS

In this section, the use of cointegration to remove or at least mitigate the influence of EOVs is examined with a simulated case study. The training and testing observations are taking for the last scenario of the the simulated case 3 in section 3.1.3, whose results are shown in figure 3.14. In this scenario, the undamped eigenfrequencies are used as feature and abnormal temperature variations are present in the testing observations.

To compute the cointegrated vector $\boldsymbol{\beta}$, the feature vectors from the training observations are grouped into the feature matrix $\mathbf{X}_{tr} \in \mathbb{R}^{nxn_{tr}}$, where $n = 10$ is the number of system's ω_n and $n_{tr} = 200$ the number of training observations.

Following the instructions stated in section 2.3.4, each row of $\mathbf{X}_{tr}$ is verified to be $I(1)$ whit the ADF test. Then, they are tested for cointegration applying the Lag Option 1 and Lag Option 2 procedures. The range of $k \in [3,\ 14]$ is computed from equation 2.17. Two cointegrating vectors are obtained, one for each option.

For both options, the cointegrated residuals for the training, testing undamaged and testing damaged observations ($\mathbf{z}_{tr}$,$\mathbf{z}_{te}$,$\mathbf{z}_{d1}$ and $\mathbf{z}_{d2}$) are computed applying equation 2.16. In that equation the corresponding feature matrix ($\mathbf{X}_{tr}$,$\mathbf{X}_{te}$,$\mathbf{X}_{d1}$ or $\mathbf{X}_{d2}$) is input as the training series $\mathbf{Y}$. The threshold value is set as the value that allows 1% of false positives outside the lower and upper threshold limits in the training observations.

The results computed from Lag Option 1 are shown in figure 3.15. The results computed from Lag Option 2 are shown in figure 3.17. The results from both options are evaluated through their performance indicators, which are shown in table 3.1. According to them, both cointegrating vectors are able to remove the temperature variation influence in the results even for abnormal temperatures. Both of them correctly classify 100 % of testing damaged observations, and they have the same values of TPR and AUC for the testing observations being evaluated. The cointegrating vector from Option Lag 1 produces 5% of false positives and has a $t_\rho = -0.33$. However, the cointegrating vector from Option Lag 2 produces only 3% of false positives and has a $t_\rho = -0.97$. The lowest value of t_ρ means that its $\mathbf{Z}_{tr}$ is most stationary according to the ADF test. Then, it is concluded that Lag option 2 gives the most feasible cointegrating vector for this particular case study.

Table 3.1: Performance indicators of the cointegrated residuals obtained from cointegration in a range $k \in [3,\ 14]$

Option	k	t_ρ	FPR(%)	TPR(%)	AUC
Lag option 1	4	-0.33	5	100	1.00
Lag option 2	14	-0.97	3	100	1.00

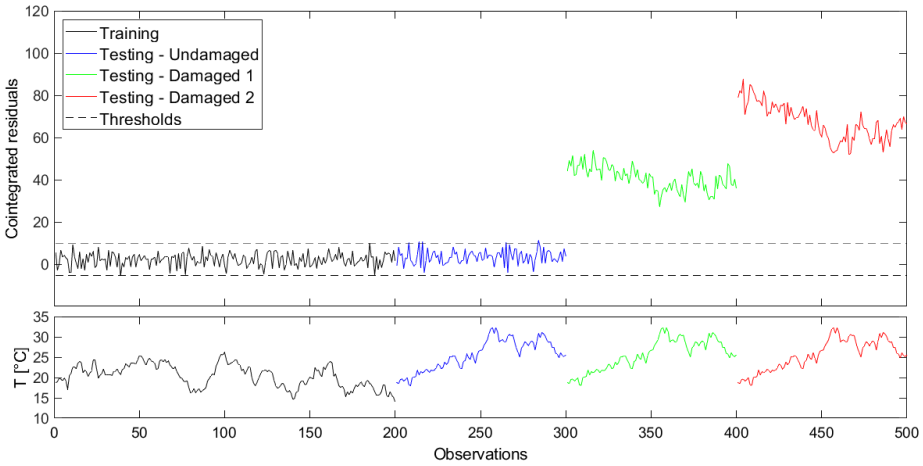

Figure 3.15: Cointegrated residuals using ω_n as feature and Lag Option 1 is used to compute the optimal cointegrated vector for $p_c = 4$. System under temperature variation influence when temperature variations for the training and testing observations have different ranges to represent abnormal temperatures in the testing observations. In the bottom the average temperature of the ten springs at each observation is displayed.

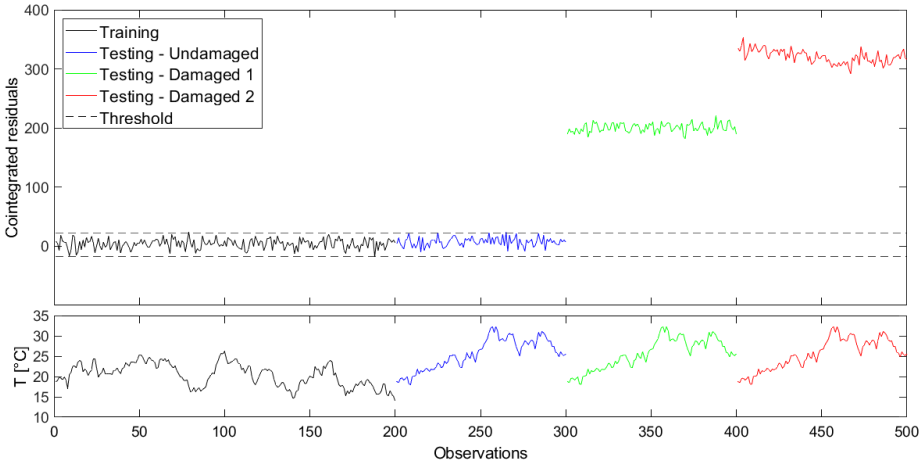

Figure 3.16: Cointegrated residuals using ω_n as feature and Lag Option 2 is used to compute the optimal cointegrated vector for $p_c = 2$. System under temperature variation influence when temperature variations for the training and testing observations have different ranges to represent abnormal temperatures in the testing observations. In the bottom the average temperature of the ten springs at each observation is displayed.

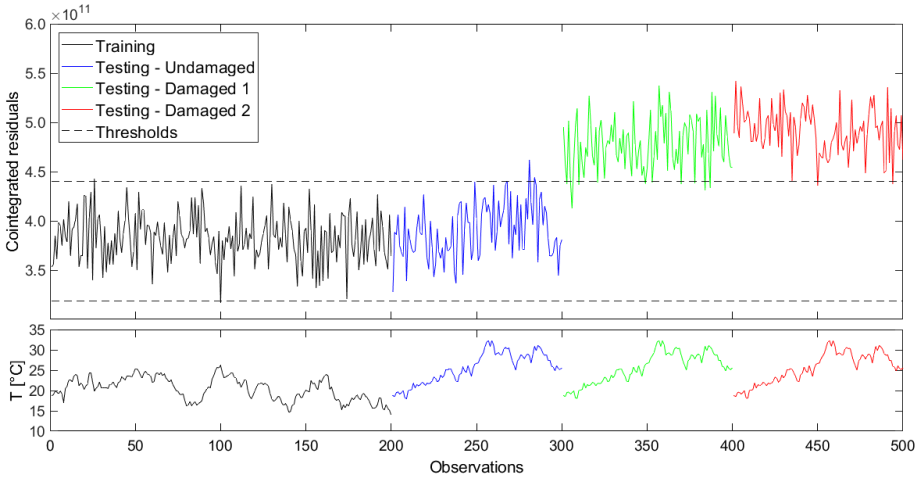

Figure 3.17: Cointegrated residuals using ω_n as feature and Lag Option 1 is used to compute the optimal cointegrated vector for $k = 28$. System under temperature variation influence when temperature variations for the training and testing observations have different ranges to represent abnormal temperatures in the testing observations. In the bottom the average temperature of the ten springs at each observation is displayed.

To evaluate if feasible cointegrating vectors can be obtained from a k value outside the range of equation 2.17, and additional cointegration is performed for a range $k \in [15, 50]$. In this range, only a suitable cointegrated vector from the Lag Option 2 is found. Their computed cointegrated residuals and performance indicators are shown in figure 3.17 and table 3.2. The performance indicators evidence that it is not better than the cointegrating vectors found before.

3.2.1 SUMMARY OF SIMULATION STUDY

The results from this simulated case show that cointegration is an effective way two remove the influence of abnormal temperature variations in the testing observations. The two options proposed to find feasible cointegrated vectors, Lag Option 1 and Lag Option 2, accomplish their purpose. The final evaluation of the cointegrated vectors can be achieved with the performance indicators. Feasible cointegrating vectors can be found from k values outside the range of equation 2.17.

Table 3.2: Performance indicators of the cointegrated residuals obtained from cointegration in a range $k \in [15, 50]$

Option	k	t_ρ	FPR(%)	TPR(%)	AUC
Lag option 1	28	-0.33	3	94	99.11

Chapter 4

EXPERIMENTAL APPLICATION

In this chapter the methods described in chapter 2 and validated in chapter 3 are applied to data from a real structure. The aim is to investigate their capability to remove or at least mitigate the EOVs' influences in the damage detection results under realistic conditions. To this end, experimental vibrational data from an operating Vestas V27 wind turbine blade are used.

The vibrational data correspond to the researches conducted in [17, 21]. In the next section, a description of the experimental setup and recorded measurements are presented.

4.1 EXPERIMENT SETUP

The Vestas V27 wind turbine is a 225 KW wind turbine with 27 m rotor diameter, and two speed regimes: 32 and 43 rotations per minute (RPM). It is a relatively old turbine with blades stiffer than the blades of modern wind turbines. However, it represents an adequate system to validate the methods being investigated in a realistic scenario.

4.1.1 INSTRUMENTATION

One of the V27 blades is instrumented with one electromechanical actuator and twelve accelerometers on its outer surfaces. Figure 4.1a) shows the accelerometers mounted in the blade, figure 4.2 illustrates their distribution and table 4.1 states their specifications. Accelerometers A1, A4, A7 and A10 are mounted about 50 mm from the leading edge. Accelerometers A2, A5, A8 and A11 are mounted about 50 mm from the trailing edge. Accelerometers A3, A6 and A9 are mounted on top of the blade spar. Accelerometer A12 is mounted near the actuator.

The actuator is mounted on the other side of the blade, see figure 4.1b). The actuator is controlled by a signal to hit the blade surface periodically. The hits introduce mechanical energy that propagates along the blade as measurable mechanical waves [21], which are the vibration responses measured by the accelerometers.

Table 4.1: Accelerometers and acquisition system specifications. Label refers to figure 4.2

Description	Quantity	Brand	Type	Sensitivity	Label
Accelerometer	1	B&K	4507-B-001	1 mV/m/s^2	A12
Accelerometer	11	B&K	4507-B-004	10 mV/m/s^2	A1 to A11

(a) (b)

Figure 4.1: Instrumented blade of Vestas V27 wind turbine. (a) Accelerometers. (b) Actuator

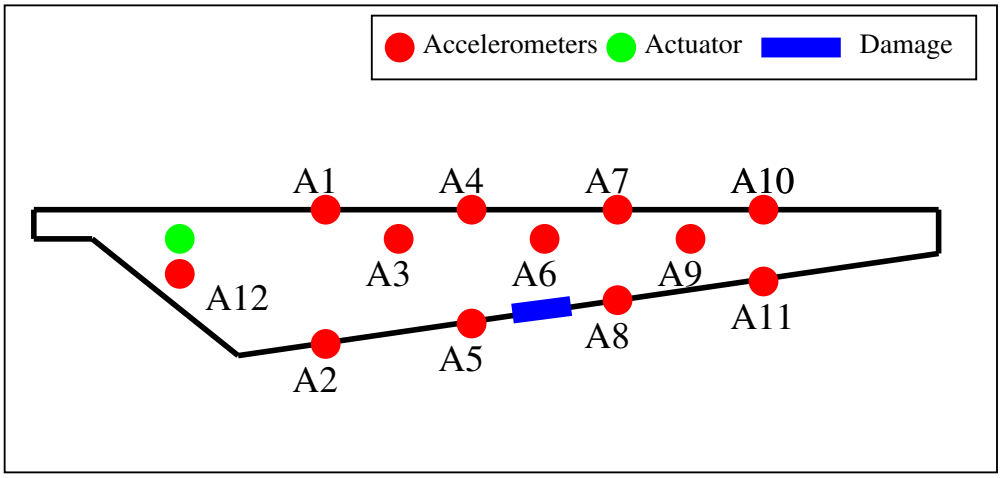

Figure 4.2: Illustration of the actuator, accelerometers and damage locations on the Vestas V27 wind turbine blade

Figure 4.3: Trailing edge opening of 30 cm to introduce damage in the blade.

4.1.2 INTRODUCTION OF DAMAGE

Four states of the wind turbine blade are tested. The undamaged state and three damaged states. Damaged states are introduced performing an opening of different sizes in the trailing edge of the blade, see figures 4.2 and 4.3. The first damaged state corresponds to an opening of 15 cm, this opening is increased to 30 cm for the second damaged state and to 45 cm for the third damage state.

4.1.3 MEASUREMENTS

Together with the actuator drive signal and the vibration response signals from the accelerometers, two signals that provide the rotor azimuth and the pitch sensor signal are recorded from the wind turbine system. The recording is done with an acquisition system installed inside the spinner. In total 16 signals with a sampled frequency of 16384 Hz are recorded with the acquisition system.

The 16 signals are recorded from 10-15 seconds before the actuator hit to 15-20 seconds after. With this, 30 seconds of each signal are recorded at each observation. Then, a record-

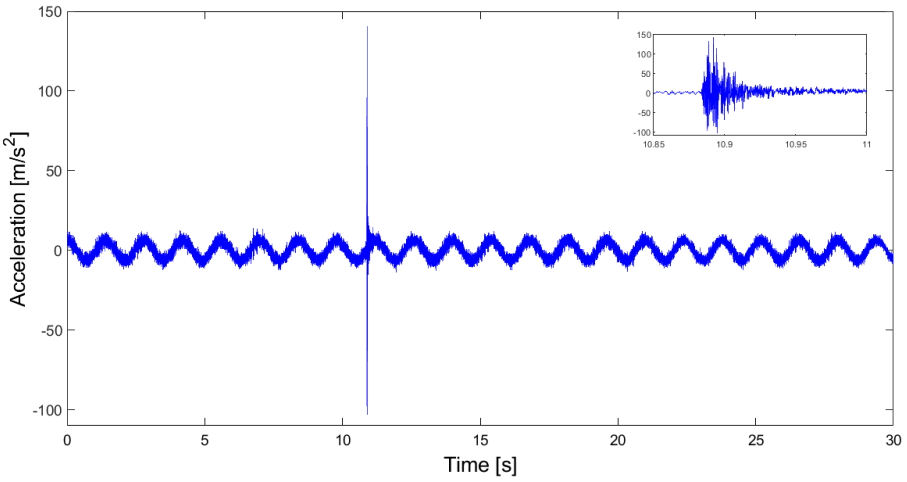

Figure 4.4: Accelerations measured in accelerometer A1 during the 53rd observation of the undamaged state. The inset plot highlights the interval of larger amplitudes.

ing of 16 measurement sequences of 491520 sample points is done at each observation.

At the same time, temperature, wind speed and direction, wind turbulence, atmospheric pressure, and precipitation measurements are collected from a meteorological mast. Also, RPM, power production and yaw angle measurements are obtained from the wind turbine system.

In the measurement campaign, observations from the wind turbine operating in the four states are collected in successive periods. The undamaged state runs from October 2014 until December 9th 2014. At that time, the first damaged state of 15 cm is introduced. On December 15th 2014, the opening is increased to 30 cm to introduce the second damaged state. The third damage state is introduced on January 4th 2015 and the turbine operates in this state until January 19th 2015.

In total, 3065, 1770, 3407 and 3722 observations are recorded from the undamaged, first, second and third damaged states, respectively. Figure 4.4 shows the accelerations corresponding to the vibration response signal in accelerometer A1 during the 53rd observation of the undamaged state.

In each state, the turbine operates under different environmental and operational conditions. Figure 4.5 shows the RPM, temperature and wind speed corresponding to the undamaged state observations.

4.2 DAMAGE DETECTION

Damage detection is performed in four steps. First, in the cleansing step, the vibration response signals are prepossessing to obtain the data to be analysed. Second, features are extracted from the Fast Fourier Transform (FFT) of the cleansed vibration responses. Third,

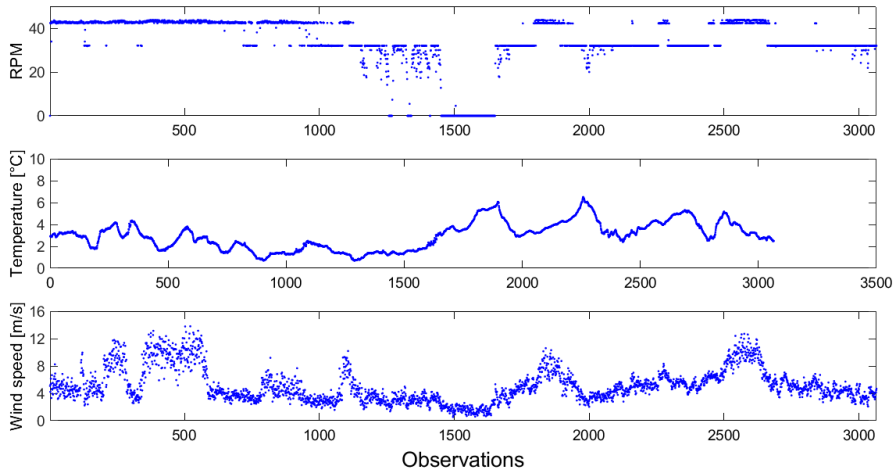

Figure 4.5: RPM, temperature and wind speed recorded from all observations of the undamaged state.

the Mahalanobis square distances from the features associated with each accelerometer are computed. These Mahalanobis square distances are used as advanced features for the next step. Fourth, a cointegrated residual metric-based outlier analysis approach is applied to the advanced features to conduct damage detection.

To assess if the described damage detection procedure is capable of remove or at least mitigate the EOVs' influence in the results, the training observations in steps three and four are taken only from the 43 RPM regime of the wind turbine. However, the testing undamaged and damaged observations are taken from both 32 and 43 RPM regimes. As a result of this selection, the testing observations from the 32 RPM regimen represent abnormal operational conditions.

4.2.1 DATA CLEANSING

The 32 RPM regime is defined, in this case study, as the observations where the wind turbine operates at RPM $\in [30, 34]$. Likewise, the 43 RPM regime is defined as RPM $\in [41, 45]$. Only observations that correspond to these regimes are selected from the whole observations of each state.

The observations are grouped into five sets, n_{tr} training observations, n_{te} testing undamaged observations, n_{d1} testing damaged-1 observations, n_{d2} testing damaged-2 observations, and n_{d3} testing damaged-3 observations.

For the training observations, $n_{tr} = 500$ observations of 43 RPM from the undamaged state are extracted. For the testing undamaged observations, 300 additional observations of 43 RPM and 300 observations of 32 RPM were extracted from the undamaged state, giving in total $n_{te} = 600$ observations. For the testing damaged-1 observations, 79 observations of 32 RPM and 100 observations of 43 RPM were extracted from the first damaged state,

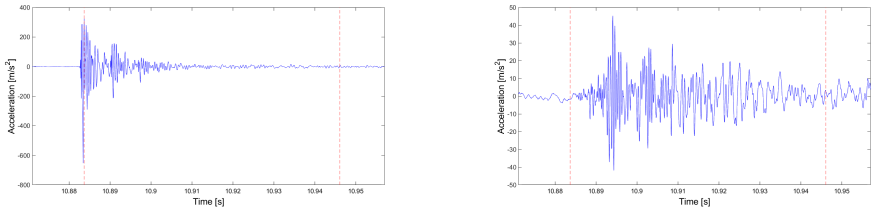

(a) (b)

Figure 4.6: Segment of vibration response signals from the 53rd observation of the undamaged state. The extracted interval is shown between red dashed lines. The dashed line on the left is the time reference use to align the twelve signals of this observation. (a) Accelerometer A12. (B) Accelerometer A8.

giving in total $n_{d1} = 179$ observations. For the testing damaged-2 and testing damaged-3 observations, 100 observations of each RPM regime were extracted from the second and third damaged sates respectively, giving in total $n_{d2} = 200$ and $n_{d3} = 200$ observations. Thus, the training observations only correspond to 43 RPM, while the testing observations correspond to both RPM regimes.

In the measurement campaign, the recorded 30 seconds of the vibration response signals are not obtained with a specific reference time. As it is stated in subsection 4.1.3, the recording started 10 to 15 seconds before the actuator hit. Therefore, the vibration response signals among the observations need to be aligned with the same reference. The actuator drive signal is a measure of the input to the actuator, but not of its output. Since the accelerometer A12 is near the actuator, the maximum peak amplitude of the vibration response signals measured by it can be taken as an indication of the actuator hit. Then, the time at which this maximum peak occurs is taken as the time reference to extract the required sample points from the vibration response signals measured by the twelve accelerometers at each observation.

At each observation, the time reference is found. From this time reference, $n_t = 1024$ sample points are extracted from the vibration response signals measured by the twelve accelerometers. The selection of that number of sample points to be extracted is done for two reasons. First, this interval corresponds to the period of time where the vibration responses induced by the actuator hit are predominant. Second, a number equal to a power of 2 is recommended to increase the performance of the FFT algorithm [8]. Figure 4.6 shows between reed lines the extracted interval from the vibration response signals of accelerometers A12 and A8. These vibration response signals correspond to the 53rd observation of the undamaged state.

Finally, the mean of each extracted interval is removed, and the data is stored. For each of the five sets of observations, the cleansed vibration responses are stored in twelve matrices $\mathbf{Y}_j \in \mathbb{R}^{n_t \times n_o}\ \forall j \in [1,\ 12]$. There, n_t is the number of extracted sample points, and n_o represents the number of observations of each set: n_{tr}, n_{te}, n_{d1}, n_{d2} or n_{d3}. Each matrix corresponds to one accelerometer, and each column of $\mathbf{Y}_j$ is the vibration response from a particular observation measured by a specific accelerometer j: $\mathbf{y}_j \in \mathbb{R}^{n_t}\ \forall j \in [1,\ 12]$.

4.2.2 FEATURE EXTRACTION

The feature selected is the combination of the real and imaginary parts of the complex Fourier coefficients obtained from the FFT algorithm. The FFT of each vibration response $\mathbf{y}_j$ is computed from the five sets of observations. The n_t complex Fourier coefficients are obtained, but these coefficients are unique only up to $\frac{n_t}{2}$ [8]. Therefore, only half of them are used to obtain the feature. These coefficients are stored in the complex vector $\mathbf{c}_j \in \mathbb{C}^{\frac{n_t}{2}}\ \forall j \in [1,\ 12]$. The complex vector $\mathbf{c}_j$ can be represented as $\mathbf{c}_j = \mathbf{a}_j + i\mathbf{b}_j$, where $\mathbf{a}_j$ and $\mathbf{b}_j \in \mathbb{R}^{\frac{n_t}{2}}\ \forall j \in [1,\ 12]$. The feature $\mathbf{x}_j \in \mathbb{R}^p\ \forall j \in [1,\ 12]$, where $p = n_t$ is the feature dimension , is obtained from equation 4.1.

$$\mathbf{c}_j = \mathbf{a}_j + i\mathbf{b}_j \quad \rightarrow \quad \mathbf{x}_j = \begin{bmatrix} \mathbf{a}_j \\ \mathbf{b}_j \end{bmatrix} \tag{4.1}$$

From the five sets of observations, the associated training, testing undamaged, testing damaged-1, testing damaged-2 and testing damaged-3 features are obtained. Each set of features is stored in twelve matrices $\mathbf{X}_j \in \mathbb{R}^{n_t \times n_o}\ \forall j \in [1,\ 12]$. Each matrix contains the features associated with a specific accelerometer j.

4.2.3 MAHALANOBIS METRIC-BASED OUTLIER ANALYSIS

Equation 2.2 is rewritten employing the variables being used, in this section, in equation 4.2. This equation is used to compute the Mahalanobis square distances from the features associated with each accelerometer from the five sets of observations.

$$d_j = \left(\mathbf{x}_j - \overline{\mathbf{x}}_{tr_j}\right)^T \left[\mathbf{S}_{tr_j}\right]^{-1} \left(\mathbf{x}_j - \overline{\mathbf{x}}_{tr\,j}\right) \tag{4.2}$$

The mean $\overline{\mathbf{x}}_{tr_j}$ and covariance matrix $\mathbf{S}_{tr_j}$, in equation 4.2 are computed from the n_{tr} training features. Then, one Mahalanobis square distance d_j is obtained from each testing feature $\mathbf{x}_j$. For each set of observations, the Mahalanobis square distances are stored in twelve vectors $\mathbf{d}_j \in \mathbb{R}^{1 \times n_o}\ \forall j \in [1,\ 12]$. Each vector is associated with a specific accelerometer j.

To investigate the performance of the computed Mahalanobis distances for damage detection, Mahalanobis metric-based outlier analysis is performed. The threshold is defined for a false positive allowance of 1% in the testing observations. Figure 4.7 shows the results associated with accelerometer A8, and figure 4.8 their ROC. The performance indicators are FPR=48.5%, TPR=100% and AUC = 0.99. Figure 4.9 show the results associated with accelerometer A9, and figure 4.10 their ROC. In this case the FPR = 0.5%, but the TPR = 6.6%, and the AUC = 0.65. The results corresponding to all accelerometers are summarized in table 4.2. The influences of the abnormal temperatures and RPMs in the testing undamaged observations can be appreciate in figure 4.7. Mahalanobis squares distances from the accelerometers located in the trailing edge have TPR s = 100%, but with FPRs $\geqslant$32.2%, see table 4.2. The results associated with the accelerometers in the spar appear to not follow the temperature and RPM trends, but they have the worst performance with TPR $\leqslant$67.5%. From

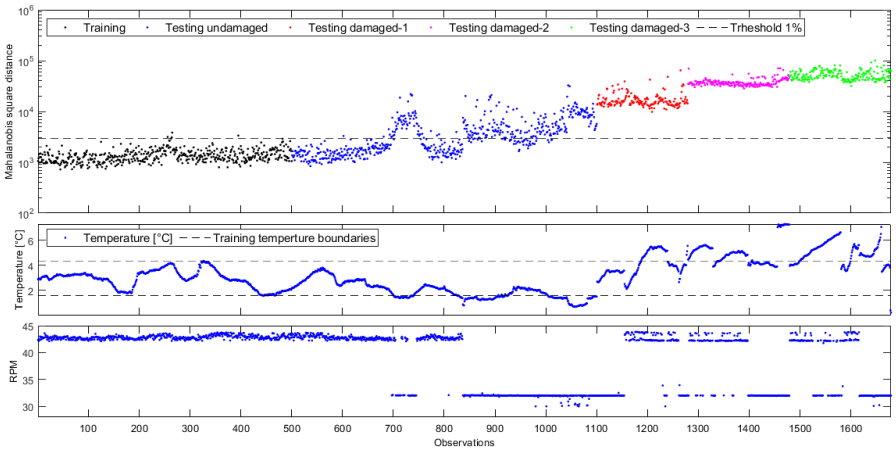

Figure 4.7: Mahalanobis square distances associated with accelerometer A8, and temperature and RPM at each observation

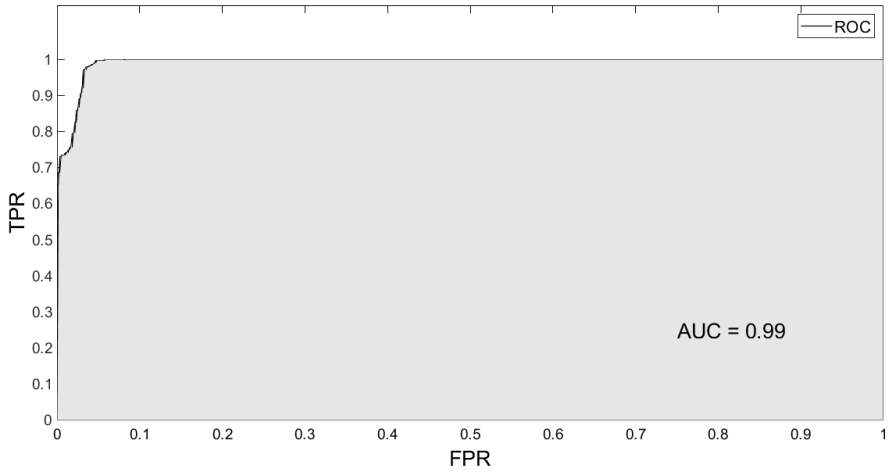

Figure 4.8: ROC from Mahalanobis square distances associated with accelerometer A8

the Mahalanobis square distances and performance indicators results, it is clear that the Mahalanobis square distances alone can not remove the influence of the abnormal temperatures and RPMs.

The Mahalanobis square distances results are compared with the all environmental and operational measured conditions available in the data: temperature, wind speed, wind direction, precipitation, RPM, rotor azimuth, pitch angle, yaw angle and power production. It is observed that the driven EOVs are the temperature and RPM, which is in agreement with what is stated in [19].

Table 4.2: Performance indicators from the Mahalanobis squares distances results

	Trailing edge				Leading edge				Spar			
	A2	A5	A8	A11	A1	A4	A7	A10	A3	A6	A9	A12
FPR (%)	47.0	50.7	48.5	32.2	29.2	26.0	45.3	5.7	31.8	6.2	0.5	27.5
TPR(%)	100	100	100	100	70.3	83.2	95.3	77.0	67.5	66.1	6.6	86.4
AUC	0.88	0.96	0.99	0.99	0.81	0.86	0.91	0.93	0.78	0.89	0.65	0.87

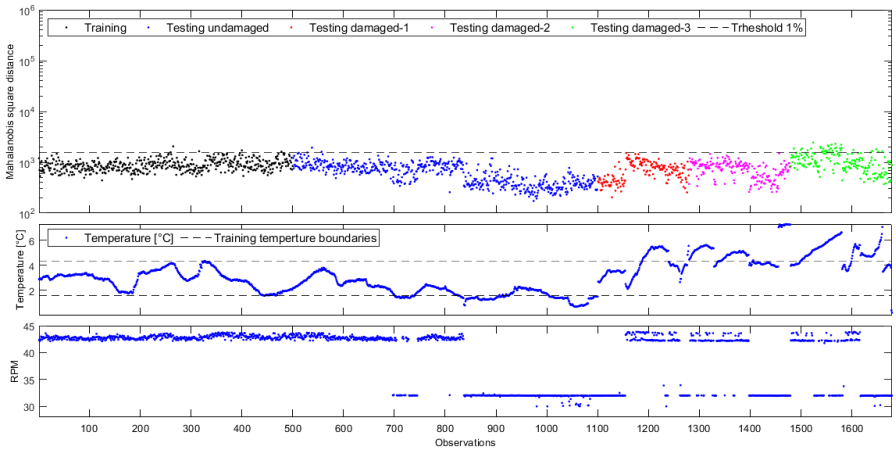

Figure 4.9: Mahalanobis square distances associated with accelerometer A9, and temperature and RPM at each observation.

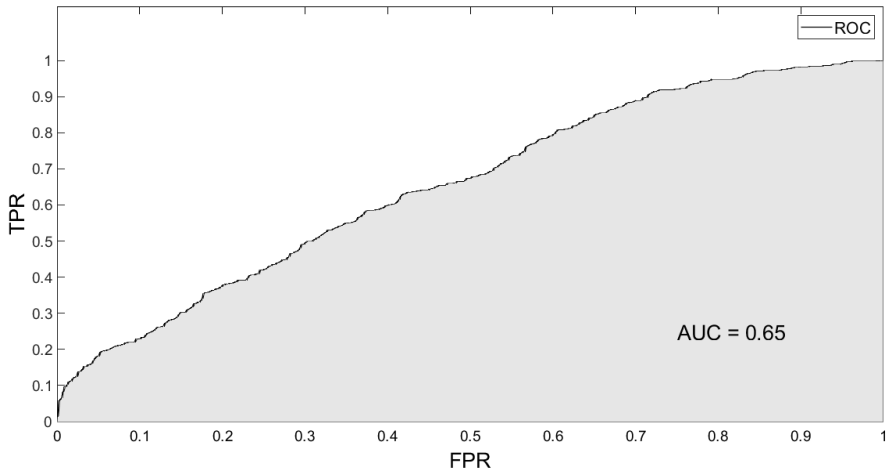

Figure 4.10: ROC from Mahalanobis square distances corresponding to accelerometer A9

4.2.4 COINTEGRATION METRIC-BASED OUTLIER ANALYSIS

The Mahalanobis square distances associated with each accelerometer from the five set of observations $\mathbf{d}_j \in \mathbb{R}^{1\times n_o}\ \forall j \in [1,\ 12]$ are used to construct advanced features associated with each observation. A cointegration metric-based outlier analysis is performed with these advanced features.

The twelve $\mathbf{d}_j \in \mathbb{R}^{1\times n_{tr}}$, from the set of n_{tr} training observations, are grouped into a training advanced feature matrix $\mathbf{X}'_{tr} \in \mathbb{R}^{p\times n_{tr}}$, where each column is the advance feature associated with a particular observation, $p = n = 12$ is the dimension of the advanced feature, and each row $\mathbf{x}'_{tr_i} \in \mathbb{R}^{1\times n_{tr}}\ \forall i \in [1,\ 12]$ corresponds to the $\mathbf{d}_j$ associated with a specific accelerometer according to equation 4.3.

$$\mathbf{x}'_{tr_i} = \mathbf{d}_j; \quad \forall i = j \in [1,\ 12] \tag{4.3}$$

Following the cointegration steps, section 2.3.4, each $\mathbf{x}'_{tr_i}$ is verified to be $I(1)$. Next, the the procedures Lag option 1 and Lag option 2 are following to search for feasible cointegrating vectors.

In the same way as for $\mathbf{X}'_{tr}$, the twelve $\mathbf{d}_j$ for the n_{te} testing undamaged, n_{d1} testing damaged-1, n_{d2} testing damaged-2, and n_{d3} testing damaged-3 set of observations are grouped to obtain the corresponding advanced feature matrices $\mathbf{X}'_{te}$, $\mathbf{X}'_{d1}$, $\mathbf{X}'_{d2}$ and $\mathbf{X}'_{d3}$. Then the cointegrated residuals associated with each set of observations ($\mathbf{z}_{tr}$, $\mathbf{z}_{te}$, $\mathbf{z}_{d1}$, $\mathbf{z}_{d2}$ and $\mathbf{z}_{d3}$) are computed with equation 2.16 for Lag Option 1 and Lag Option 2.

Table 4.3 is the summary of the performance indicators from both options when lag values $k \in [3,\ 17]$, obtained from equation 2.17, are used for the Johansen procedure. In that case, two cointegrating vectors $\boldsymbol{\beta}$, one from each option, are found. From Lag Option 1, a feasible cointegrating vector with $k = 17$ is found. From Option 2 a feasible cointegrating vector from the same k is found. The best performance corresponds to Lag Option 2, which classify correctly 94.82% of the damaged observation giving 19.67% of false positives for 1% threshold. Also, its $\mathbf{z}_{tr}$ is most stationary according to the ADF test, because its t_ρ is the most negative. It must be noted, that from the ADF test, the most stationary $\mathbf{z}_{tr}$ is not associated with the highest eigenvalue of the Johansen procedure from a $k = 7$. Figure 4.11 and figure 4.12 show the cointegrating residuals and ROC obtained from Lag Option 2 results.

An inspection of figure 4.11 reveals that the classification of the testing damaged-3 observations, with the $\boldsymbol{\beta}$ from Option Lag 2, is poor. The 54% of the testing damaged-3 observations are classified as true positives because they are under the lower threshold limit. Furthermore, if its $\mathbf{z}_{tr}$ is compared with the temperatures and RPMs in figure 4.7, it can be appreciated the influence of the EOVs in the testing undamaged observations.

To investigate if a more suitable cointegrating vector can be found, the cointegration procedure is performed for other range of values $k \in [18,\ 50]$. Table 4.4 presents the performance indicators from the results of both Lag Options. It can be seen that the results from Lag Option 1 with $k = 36$ have the best performance indicators.

Table 4.3: Performance indicators of the cointegrated residuals obtained from cointegration in a range $k \in [3,\ 17]$

Option	k	t_ρ	FPR(%)	TPR(%)	AUC
Lag option 1	17	-3.52	21.33	94.99	0.964
Lag option 2	17	-7.79	19.67	94.82	0.964

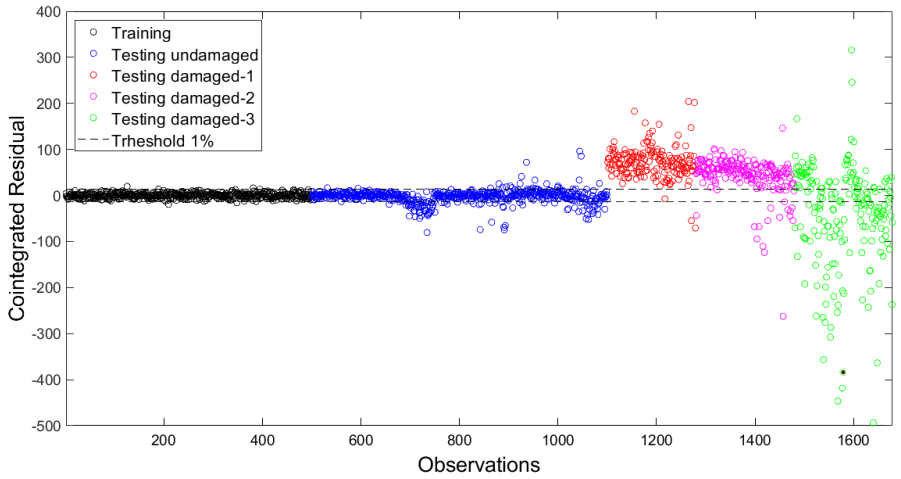

Figure 4.11: Cointegrated residuals from Option Lag 2 and lag value $k = 17$, with Mahalanobis square distances as advanced feature.

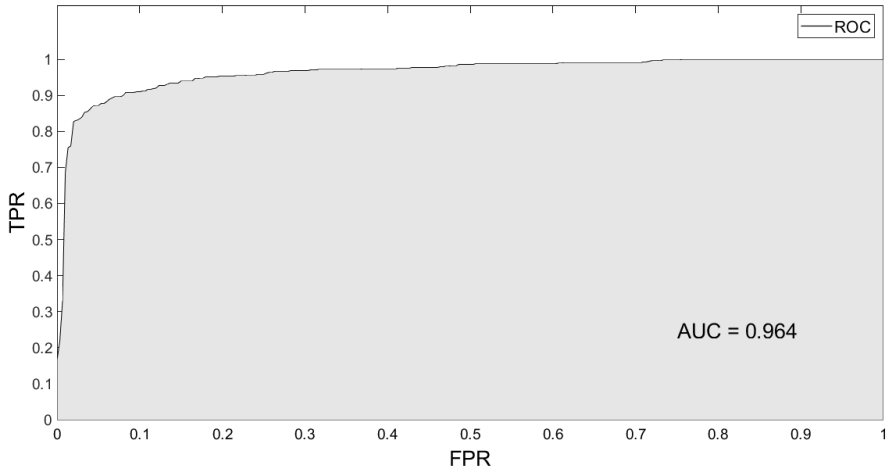

Figure 4.12: ROC from cointegrated residuals computed with Lag Option 2 and lag value $k = 17$

Table 4.4: Performance indicators of the cointegrated residuals obtained from cointegration in a range $k \in [18, 50]$

Option	k	t_ρ	FPR(%)	TPR(%)	AUC
Lag option 1	36	-7.93	15.17	100	0.998
Lag option 2	23	-8.73	41.50	99.31	0.968

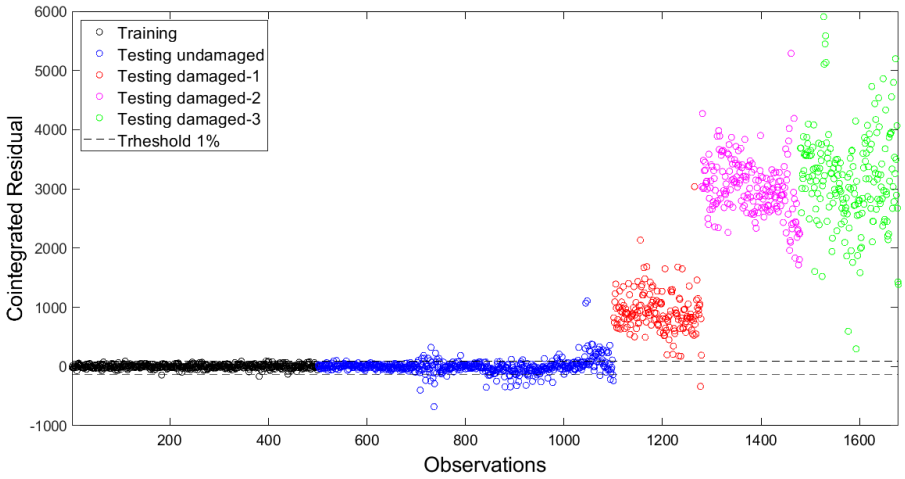

Figure 4.13: Cointegrated residuals from Option Lag 1 and lag value $k = 36$, with Mahalanobis square distances as advanced feature.

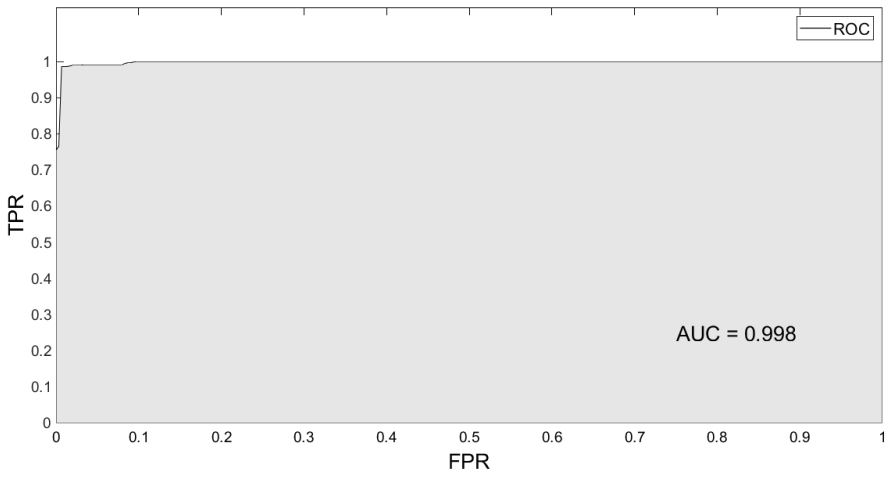

Figure 4.14: ROC from cointegrated residuals computed with Lag Option 1 and lag value $k = 36$

The β from Lag Option 1 and $k = 36$ correctly classifies the 100% of the testing damaged observations with 15.17% of false positives for a 1% threshold, see table 4.4. Its cointegrated residuals and corresponding ROC are shown in figures 4.13 and 4.14. It performs almost a

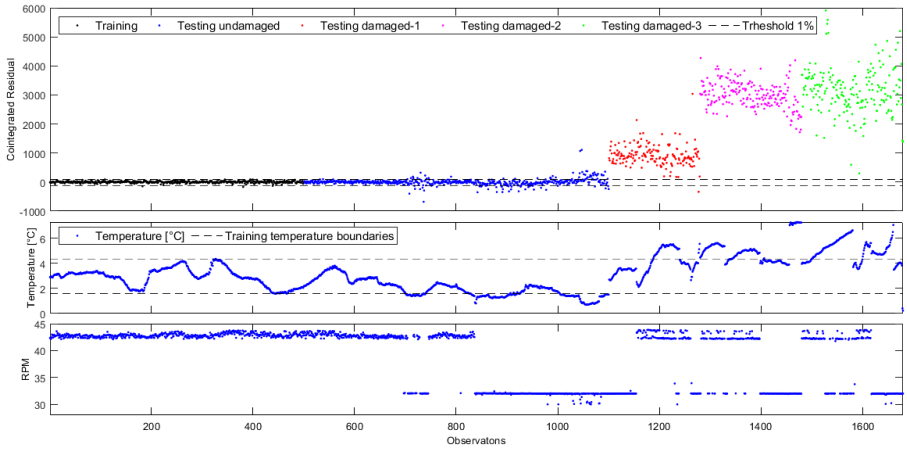

Figure 4.15: ROC from cointegrated residuals computed with Lag Option 1 and lag value $k = 36$

perfect classification with an AUC=0.998, despite it does not give the most stationary $\mathbf{z}_{tr}$ according to its t_ρ. The EOVs' influences in the testing undamaged observations have been mitigated. Consequently the Lag Option 1 with $k = 36$ gives the most suitable $\boldsymbol{\beta}$ for the outlier analysis of this experimental case study.

From figure 4.13, it is seen that, the cointegrated vector from Lag Option 1 and $k = 36$ is able to differentiate the testing damaged-1 observations from the testing damaged-2 and testing damaged-3 observations. However it can not differentiate between the two latter sets of testing damaged observations. Also, the remaining EOVs' influence in its testing undamaged observations are observed to be driven, as in the case of the Mahalanobis square distances, by the abnormal temperatures and RPMs, see figure 4.15.

Chapter 5

DISCUSSION AND CONCLUSIONS

5.1 DISCUSSION

In the Johansen procedure, the most stationary cointegrated residual is obtained with the cointegrating vector associate with the largest eigenvalue [2]. However, this cointegrated residual is not necessarily the most stationary when the ADF test is applied. Furthermore, the aim of applying the Johansen procedure is to find a cointegrating vector that reaches two goals. First, it should generate cointegrated residuals that remain stable between certain limits from features that correspond to the reference state of the structure [2]. Second, the generated cointegrated residuals should be damage sensitive without or little EOVs influences. Then, find the most stationary residual is not a priority for a SDD approach. Consequently, the use of other cointegrating vectors do not associate with the largest eigenvalue, should not be discarded.

Although the formula 2.17 recommended in [4] to set the maximum number of lags to be included in the Johansen procedure is an acceptable start. Suitable cointegration vectors can be found when higher numbers of lags are used.

5.2 CONCLUSIONS

It has been demonstrated, through simulated and experimental case studies, that cointegration can mitigate the influence of EOVs in the results of a SDD approach. Nevertheless, its application is not a straightforward process. It relies on assumptions for the mathematical techniques that need to be taken into consideration during its implementation. Additionally, the selection of the feature and required parameters, as the lag values, is an interactive process that must be tailored to each application.

The procedure Option Lag 2 has proved to found feasible cointegrating vectors, which must be taken into consideration for the cointegration metric-based outlier analysis. This procedure selects a cointegrating vector from all the eigenvectors obtained from the Johansen procedure. The selection is based on the stationarity of their residuals, which is

assessed with the ADF test.

The vibration-based SDD approach presented in the experimental case is able to detect the three damage states. An advantage of this approach is that it does not require signal filtering in the cleansing step. Nevertheless, the approach is not able to differentiate between the last two damage states. It could be due to the presence of the highest abnormal temperature variations in combination with abnormal RPM in the third damage state. Or due to other unmeasured EOVs. In [21] a clear identification of the three damage states was made employing only observations from the 43 RPM regime. However, the use of observations only from the 43 RPM regime will invalidate the aim of the present study.

5.3 FUTURE WORK

Future research could be done to investigate if signal filtering can improve the results of the vibration-based SDD approach presented in the experimental case study. Also, the influence of the selection of a different set of training observations as observations from both RPM regimens or for a specific range of temperatures could be investigated. Additionally, the influence of the selection of other interval from the acceleration time series responses signals can be investigated.

BIBLIOGRAPHY

[1] E. J. Cross and K. Worden. “Cointegration and why it works for SHM”. In: *Journal of Physics: Conference Series*. Vol. 382. 1. IOP Publishing. 2012, p. 012046.

[2] E. J. Cross, K. Worden, and Q. Chen. “Cointegration: a novel approach for the removal of environmental trends in structural health monitoring data”. In: *Proceedings of the Royal Society A: Mathematical, Physical and Engineering Sciences* 467.2133 (2011), pp. 2712–2732.

[3] E. J. Cross et al. “A tutorial on cointegration for engineers—A tool for non-stationary time series analysis”. In: *Proceedings of the 10th International Conference on Recent Advances in Structural Dynamics, Southampton, UK*. July 2010.

[4] P. B. Dao, W. J. Staszewski, and A. Klepka. “Stationarity-Based Approach for the Selection of Lag Length in Cointegration Analysis Used for Structural Damage Detection”. In: *Computer-Aided Civil and Infrastructure Engineering* 32.2 (2017), pp. 138–153.

[5] Ch. Farrar and D. Jauregui. *Damage detection algorithms applied to experimental modal data from the I-40 bridge*. Tech. rep. Los Alamos National Laboratory, NM (United States), 1996.

[6] Ch. R. Farrar, S. W. Doebling, and D. A. Nix. “Vibrationbased structural damage identification”. In: *Philosophical Transactions of the Royal Society A: Mathematical, Physical and Engineering Sciences* 359.1778 (2001), pp. 131,149.

[7] Ch. R. Farrar, H. Sohn, and K. Worden. “Data Normalization: A Key For Structural Health Monitoring”. In: *Conference title not supplied* (Jan. 2001).

[8] B. D. Hahn and D. T. Valentine. *Essential MATLAB for engineers and scientists.* 7th. Amsterdam: Academic Press.

[9] D. Y. Harvey and M. D. Todd. “Cointegration as a data normalization tool for structural health monitoring applications”. In: vol. 8348. 1. 2012, pp. 834810–834818.

[10] J. Hunter, S.P. Burke, and A. Canepa. *Multivariate Modelling of Non-Stationary Economic Time Series*. Elektronisk udgave. -2nd ed. 2017. Palgrave Texts in Econometrics. London: Palgrave Macmillan UK.

[11] D. J. Inman. *Engineering Vibration*. International ed of 4th revised ed. Pearson, 2014.

[12] G. Chr. Larsen et al. “Effect of a Damage to Modal Parameters of a Wind Turbine Blade”. In: *EWSHM - 7th European Workshop on Structural Health Monitoring*. 2014.

[13] B. Pfaff. *Analysis of Integrated and Cointegrated Time Series with R*. Tech. rep.

[14] B. A. Qadri et al. “Cointegration for Detecting Structural Blade Damage in an Operating Wind Turbine: An Experimental Study”. In: *Proceedings of the 37th IMAC, A Conference and Exposition on Structural Dynamics 2019*. Vol. 2. Springer, 2019, pp. 173–180.

[15] H. Sohn. “Effects of Environmental and Operational Variability on Structural Health Monitoring”. In: *Philosophical Transactions: Mathematical, Physical and Engineering Sciences* 365.1851 (2007), pp. 539–560.

[16] H. Sohn et al. “Structural health monitoring using statistical pattern recognition techniques”. In: *J. Dyn. Sys., Meas., Control* 123.4 (2001), pp. 706–711.

[17] D. Tcherniak and L. L. Mølgaard. “Active vibration-based structural health monitoring system for wind turbine blade: Demonstration on an operating Vestas V27 wind turbine”. In: *Structural Health Monitoring* 16.5 (2017), pp. 536–550.

[18] E. S. Tomé, M. Pimentel, and J. Figueiras. “Damage detection under environmental and operational effects using cointegration analysis – Application to experimental data from a cable-stayed bridge”. In: *Mechanical Systems and Signal Processing* 135 (2020).

[19] T. UBull1, M. D. Ulriksen1, and D. Tcherniak. “The effect of environmental and operational variabilities on damage detection in wind turbine blades”. In: *9th European Workshop on Structural Health Monitoring (EWSHM 2018), Manchester, England*. July 2018.

[20] M. D. Ulriksen. *PhD course Vibration-based Structural Health Monitoring: Damage Detection I*. Dept. of Energy Technology, Aalborg University, Denmark, Aug. 2019.

[21] M. D. Ulriksen, D. Tcherniak, and L. Damkilde. “Damage detection in an operating Vestas V27 wind turbine blade by use of outlier analysis”. In: *2015 IEEE Workshop on Environmental, Energy, and Structural Monitoring Systems (EESMS) Proceedings*. 2015, pp. 50–55.

[22] K. Worden, G. Manson, and N.R.J Fieller. “Damage detection using outlier analysis”. In: *Journal of Sound and Vibration* 229.3 (2000), pp. 647–667.

[23] K. Worden et al. “The fundamental axioms of structural health monitoring”. In: *Proceedings: Mathematical, Physical and Engineering Sciences* 463.2082 (2007), pp. 1639–1664.